Dissertation

Optimization of contrast agent application protocols in pediatric thoracic computer tomography

submitted by

Dr. med. Eszter Nagy

for the Academic Degree of

Doctor of Medical Science (Dr. scient. med.)

at the

Medical University of Graz

Department of Radiology, Division of Pediatric Radiology

under the supervision of

Univ.-Prof. DDr.hc.med.univ. Erich Sorantin

Priv.-Doz. Dr.med.univ. Peter Kalmar, MHBA

Priv.-Doz. Dr.med.univ. Andreas Pfleger

2020

I dedicate this work to my beloved husband,
András, who continuously encouraged, helped,
and stood by me.

Statutory declaration

I hereby declare, that this thesis is my original work, and I have fully acknowledged by name all of those individuals and organizations who have contributed to the research for this thesis. Due acknowledgment has been made in the text to all other material used. Throughout this thesis and in all related publications I followed the "Standards of Good Scientific Practice and Ombuds Committee at the Medical University of Graz."

Graz, 19th of August 2020

Disclosures

This thesis reproduces parts of the following publications, all authored by the doctoral candidate:

Nagy, E; Tschauner, S; Marterer, R; Riedl, R; Sorantin, E Chest CTA in children younger than two years - a retrospective comparison of three contrast injection protocols. Sci Rep. 2019; 9(1): 18109-18109.

Nagy, E; Marterer, R; Tschauner, S; Stücklschweiger, G; Sorantin, E Determination of adjusted CTA threshold to lowered tube voltage - a phantom study with tissue-mimicking materials on three CT scanners - under submission

The following co-authors actively contributed to this dissertation and authorized the use of their personal data:

DDr. Sebastian Tschauner, Division of Pediatric Radiology, Department of Radiology, Medical University of Graz, Austria

Dr. Robert Marterer, Division of Pediatric Radiology, Department of Radiology, Medical University of Graz, Austria

Dipl.-Ing. Dr. Regina Riedl, Institute of Medical Informatics, Statistics and Documentation, Medical University Graz, Austria

Univ.-Doz. Mag. Dr. Georg Stücklschweiger, Competence Center of Medical Physics and Radiation Protection, University Hospital Graz

Univ.-Prof. DDr.hc.med.univ. Erich Sorantin, Division of Pediatric Radiology, Department of Radiology, Medical University of Graz, Austria

Acknowledgments

My studies would have been impossible without the continuous guidance and support of Univ.-Prof. DDr.hc.med.univ. Erich Sorantin. He provided me the opportunity to join a great research team at the Medical University of Graz, and was always fair, enthusiastic, encouraging, and critical enough to fuel my motivation to perform high-quality research. He was always ready to help and assist me, discuss and solve problems, whenever it was needed.

I also express my most profound appreciation to both other dissertation committee members, Priv.-Doz. Dr.med.univ. Peter Kalmar and Priv.-Doz. Dr.med.univ. Andreas Pfleger. As renowned experts in their disciplines, they provided assistance and advice in many respects.

I would also like to thank my other colleagues who took part in the course of the studies, especially DDr. Sebastian Tschauner and Dr. Robert Marterer. A big thanks to all colleges of the radiotechnology for performing the CT examinations for the phantom experiments.

And last but not least, I would like to express my gratitude to my mother and my brothers for their constant support, love, and patience with me despite the distance.

The doctoral candidate performed her studies in the Doctoral School for Sustainable Health Research at the Medical University of Graz. Current thesis project did not receive any funding.

Table of contents

List of abbreviations

AA	ascending aorta
AAPM	American Association of Physicists in Medicine
Aar	aortic arch
ABT	automatic bolus tracking
ACR	Americal College of Radiology
AD	descending aorta
AEC	automatic exposure control
AKI	acute kidney injury
ALARA	„As Low As Reasonably Achievable“
ANOVA	analysis of variance
ASER	American Society of Emergency Radiology
CA	contrast agent
chILD	childhood interstitial lung disease
CLO	congenital lobar overinflation
CNR	contrast-to-noise ratio
COPD	chronic obstructive pulmonary disease
CPAM	congenital pulmonary airway malformation
CT	computed tomography
CTA	computed tomography angiography
CTDI	computed tomography dose index
DNA	deoxyribonucleic acid
DLP	dose length product

DRL	diagnostic reference level
DSCT	dual-source computed tomography
FDA	U.S. Food and Drug Administration
GE	General Electronics
GFR	glomerular filtration rate
HU	Hounsfield unit
IV	intravenous
keV	kiloelectron volt
kV	kilovolt
LA	left atrium
Li	liver
LLPV	left lower pulmonary vein
LUPV	left upper pulmonary vein
LV	left ventricle
mAs	milliamper secundum
MBT	microbolus technique
MDCT	multidetector computed tomography
MRI	magnetic resonance imaging
Mu	muscle
PT	pulmonary trunk
RA	right atrium
RLPV	right lower pulmonary vein
ROI	region of interest
RUPV	right upper pulmonary vein

RV	right ventricle
SCBT-MR	Society of Computed Body Tomography & Magnetic Resonance
SCV	superior cava vein
SNR	signal-to-noise ratio
SPR	Society of Pediatric Radiology
SSDE	size-specific dose estimation
TAPVR	total anomalous pulmonary vein retourn
US	ultrasound

Abstract

Background and Purpose: Computed tomography angiography (CTA) is a challenging task in young children. Bolus tracking is generally advised for contrast agent (CA) timing to ensure optimal image quality. The adaption of automated bolus tracking (ABT) thresholds to different tube voltages is reasonable. However, a clear methodology to achieve the adapted ABT thresholds with the maintenance of image quality is scarce. Several variants of CA application protocols are well established in the daily routine; however, a direct head to head comparison of their applicability in the pediatric routine is missing. This work aimed to provide a transparent approach to ABT threshold calculation, as well as ABT threshold values for everyday use based on phantom measurements. Furthermore, it aimed to compare different CA application protocols for cardiothoracic CTA regarding image quality and CA iodine volume in children younger than two years of age.

Methods: Phantom measurements were conducted on an Electron Density Phantom with tissue-mimicking materials at every available tube voltages of three different CT scanners. ABT thresholds were calculated by curve fitting models using linear regression. Additionally, retrospective analysis of 70 cardiothoracic CTA scans of young children (<2 years) were performed to compare three different CA application protocols: the so-called “microbolus technique” (MBT), a conventional dual-phase protocol and one with empirical bolus delay. Furthermore, an assessment of objective and subjective image quality was performed as well.

Results: ABT thresholds were calculated at different kV settings and reference thresholds with minimal differences between the CT scanners in this regard. Bland-Altman analysis ruled out any systemic inter-scanner bias. As for CA application protocols, significantly lower CA volume was applied using the MBT protocol as well as consecutively less CA-related artifacts and better image quality were achieved with the MBT.

Conclusions: The adaptation of bolus tracking threshold is essential in thoracic CTA. Using the provided method for ABT threshold calculation, a difference up to 45% might occur between ABT thresholds at 120 kV and 70 kV. Furthermore, the examined CA application protocols showed comparable performance. With the MBT a slightly better image quality was achieved using less CA volume.

Zusammenfassung

Hintergrund: Das automatische Bolustracking (ABT) ist generell für das Kontrastmitteltiming bei thorakalen CT-Angiographien (CTA) empfohlen. Sinnvollerweise sollten die ABT-Schwellenwerte an reduzierte Röhrenspannungen angepasst werden, um ein inadäquates Kontrastmitteltiming zu vermeiden. In der Literatur ist jedoch keine transparente Methode zur Schwellenwertkalkulation beschrieben. Es gibt unterschiedliche, publizierte Kontrastmittelapplikationsprotokolle (KAP), jedoch ohne entsprechende Vergleichsstudien bezüglich der erreichten Bildqualität. Ziel dieser Arbeit war einen transparenten Weg für die Schwellenwertberechnung bereitzustellen, sowie die ABT-Schwellenwerte für den täglichen Gebrauch zu bestimmen. Das zweite Ziel war, die abteilungsintern verwendeten KAP für thorakale CTA bei Kleinkindern zu vergleichen.

Material und Methoden: Zur Schwellenwertberechnung wurden Phantommessungen an drei unterschiedlichen CT-Geräten durchgeführt. Die ABT-Schwellenwerte wurden anhand dieser Phantommessungen mit linearen Regressionen berechnet. Weiters wurden die Unterschiede in den Dichtemessungen der CT-Geräte analysiert sowie die Bildqualität und die applizierte Kontrastmittelmenge evaluiert. 70 CTA mit den folgenden KAP wurden in die Analyse eingeschlossen: Mikrobolus-Protokoll (MBT, Gruppe 1), zweiphasiges Protokoll (Gruppe 2) und fixes Delay (Gruppe 3).

Resultate: Mehrere ABT-Schwellenwerte wurden bei unterschiedlichen Röhrenspannungen und Referenzschwellenwerten berechnet und es gab minimale Unterschiede zwischen den CT-Geräten. Mittels Bland-Altman-Analyse wurde ein systematischer Fehler zwischen den CT-Geräten ausgeschlossen. In der Gruppe 1 wurde ein geringeres Kontrastmittelvolumen benötigt und es gab weniger kontrastmittelbedingte Artefakte.

Schlussfolgerungen: Anhand der Phantomdichtemessungen wurde ein Unterschied von bis zu 40% zwischen den ABT-Schwellenwerten bei 120 kV und 70 kV festgestellt. Die minimale Variablität der Dichtemessungen zwischen den CT-Geräten war irrelevant bei den Schwellenwertkalkulationen, jedoch bei manchen Pathologien könnten diese Unterschiede relevant sein. Alle drei untersuchten KAP zeigten ein vergleichbares Ergebnis, jedoch das MBT-Protokoll hatte Vorteile hinsichtlich des Kontrastmittelvolumens und der Bildqualität.

1. Introduction

1.1 Cardiothoracic CT scan in children

Thoracic CT angiography (CTA) is an integral part of the diagnostic chain in several diseases in small children. In order to avoid unnecessary duplicative imaging and its associated radiation, an evidence-based rationale for the examination is essential. According to international recommendations, several primary indications are approved for pediatric thoracic CTA, as indicated in **Table 1** (1). These indications involve several acquired and congenital disorders ranging from chest wall bony changes to cardiovascular diseases. In some entities, such as in cardiac, extracardiac, or lung disorders, a complementary contrast agent (CA) application or vascular imaging with angiography is necessary.

Tracheobronchial pathologies include several entities, such as tracheomalacia, congenital tracheal stenosis, tracheal bronchus, or impacted foreign body. In case of these suspected abnormalities, CT examination is the method of choice to demonstrate the exact location and extension of the lesions (2).

Congenital lung anomalies consist of a wide spectrum of diseases with variable vascular, parenchymal, airway, or foregut components. Some malformations represent anomalies with a single parenchymal element, such as congenital lobar overinflation (CLO) or congenital pulmonary airway malformations (CPAM). Bronchial atresia (**Figure 1**) affects only the airways with passive overinflation of the distal lung. Arteriovenous malformation represents a single vascular anomaly, while pulmonary sequester (**Figure 2**) affects vascular and parenchymal structures. Hybrid lesions consist of a combination of different lesions, such as pulmonary sequester and CPAM or CPAM and bronchial atresia. Since the suspected congenital anomaly potentially involves the vascular system as well, CTA of the thoracic and upper abdominal region is necessary to depict a possible infradiaphragmatic vascular supply (3).

	CA	CTA
Chest wall abnormalities		
Developmental disorders: pectus excavatum, rib anomalies, scoliosis	-	-
Chest wall injuries	+/-	+/-
Tumors and tumor-like lesions of the chest wall	+	-/+
Extracardiac vascular disorders		
Congenital and syndromic vascular abnormalities (rings and slings)	+	+
Acquired disorders (vasculitis, pulmonary embolism)	+	+/-
Cardiac diseases	+	+
Tracheobronchial abnormalities		
Congenital abnormalities	-	-
Secondary tracheobronchial narrowing (mass, vascular anomaly etc.)	+	+
Suspected foreign body	-	-
Tracheobronchomalacia	-	-
Mediastinal masses		
Neoplasms	+	+/-
Congenital abnormalities	+	+/-
Infectious and inflammatory processes	+	-
Trauma	+	+
Lung abnormalities		
Infection, pneumonia, abscess, etc.	+/-	-
Diffuse / interstitial lung disease	-	-
Congenital pulmonary abnormalities	+	+
Malignancy	+/-	+/-
Traumatic injuries	+	+

Table 1: Common indications for thoracic CT in pediatric patients according to the international guidelines (1). Abbreviations: CA for contrast agent, CTA for CT angiography

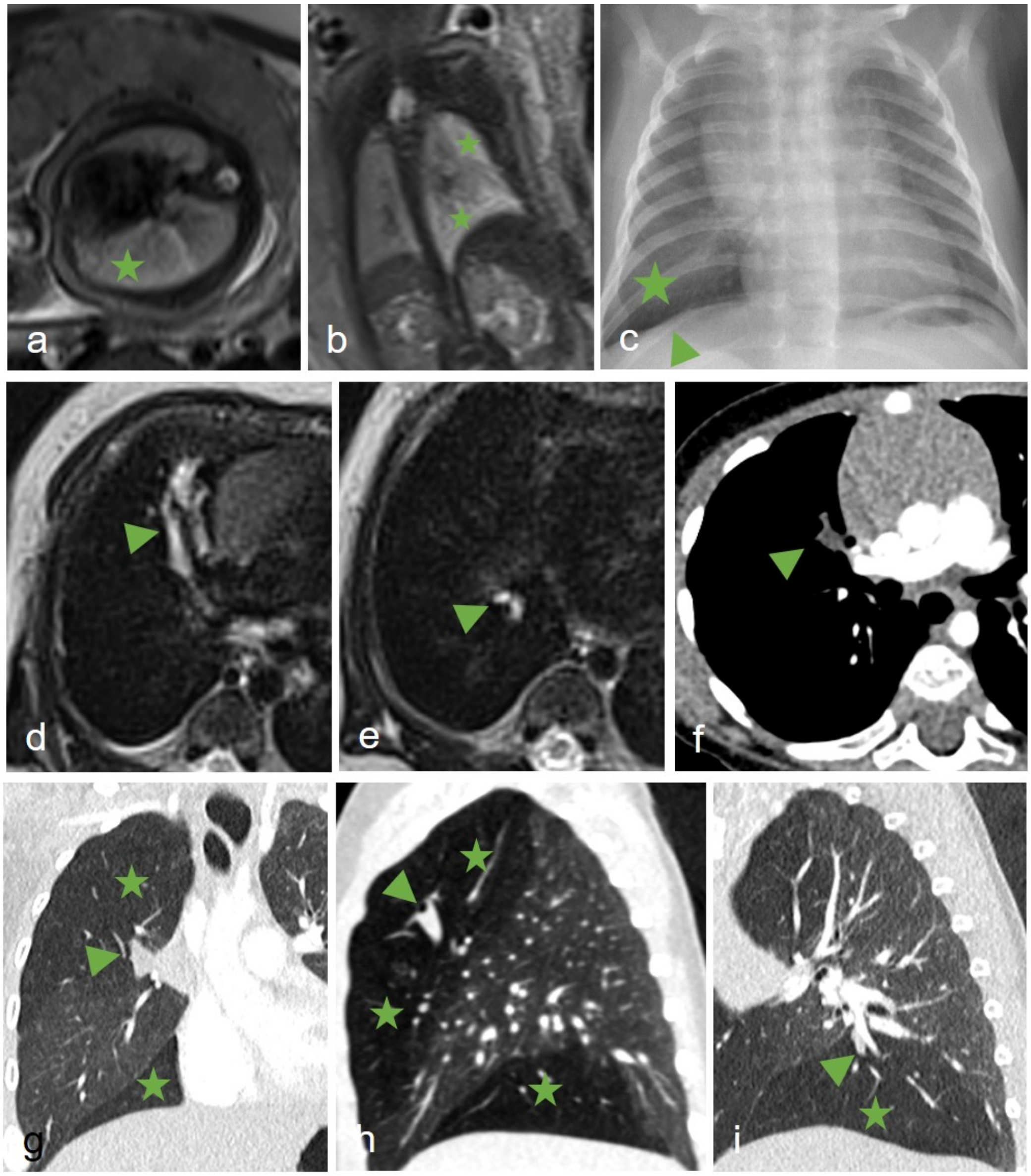

Figure 1: A 33-year-old woman subjected to fetal magnetic resonance imaging (MRI) in the 28th week of pregnancy with suspected fetal pulmonary pathology. Images of fetal MRI (**a**, **b**) showed a mediastinal displacement and an increased signal intensity of the upper and lower part of the right lung (stars on image **b**), raising the suspicion of congenital lobar overinflation. After an uncomplicated delivery, the newborn did not present any dyspnea. The routine chest x-ray (**c**) showed increased transparency on the right side (star) with a flattened diaphragm (arrowhead). On the 5th postpartal day, a feed-and–wrap MRI (**d**, **e**) showed an increased signal intensity along the bronchial tree in the right upper and lower lobes (arrowheads). Six months later, a CT angiography was performed (**f – j**), which showed a focal obliteration of a lobar bronchus in the right upper lobe (arrowheads on images **f**, **g**, and **h**) and right lower lobe (arrowhead on image **j**) with consecutive hyperinflation of the distal lung (stars on images **f**, **h**, and **j**). The findings were consistent with bronchial atresia.

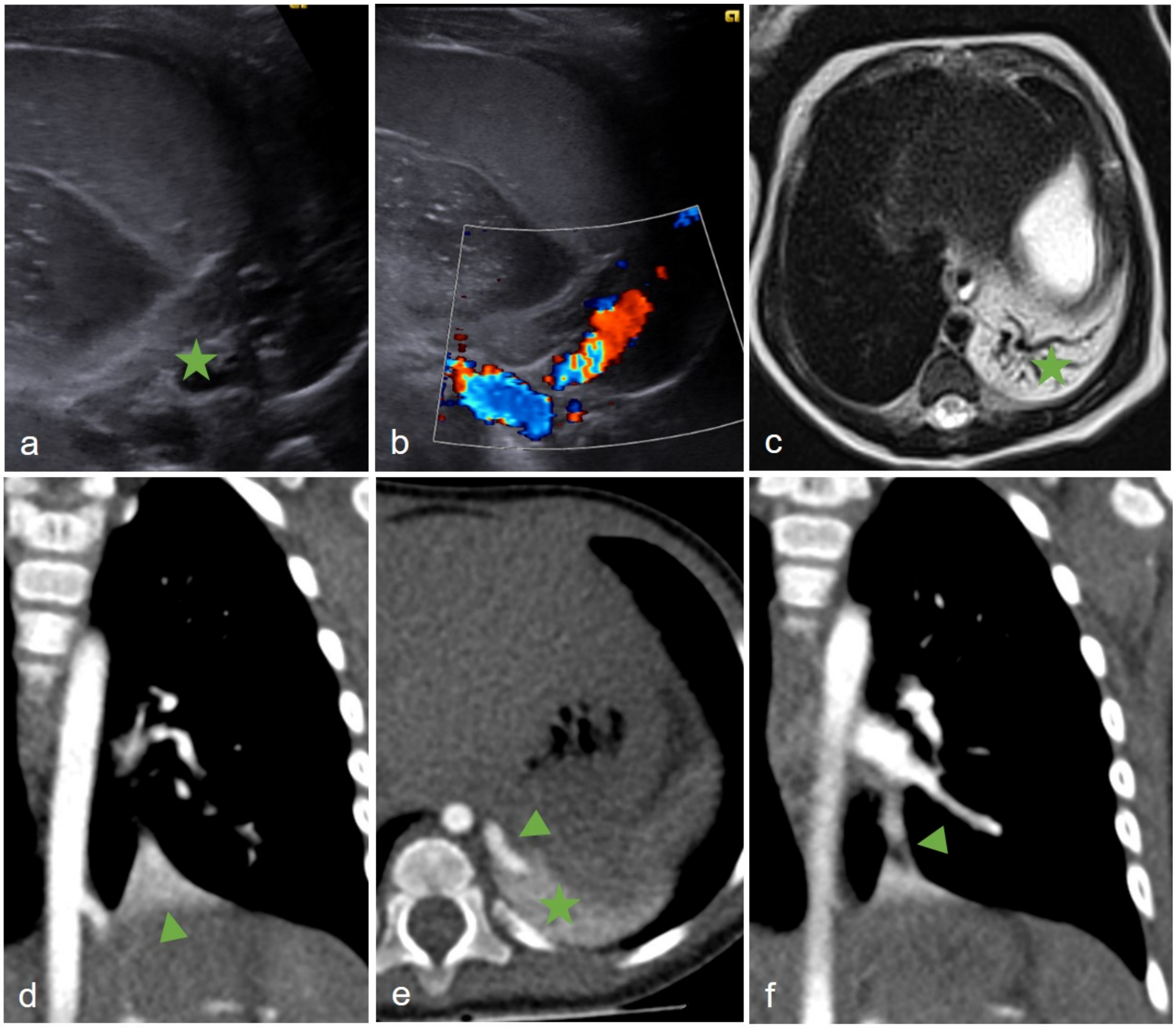

Figure 2: Three days old term baby with prenatally suspected pulmonary malformation. The initial sonography (**a**) showed a heterogeneous mass in the left lower lobe (star) with a large vascular supply on the Doppler sonography (**b**). The feed-and-wrap magnetic resonance imaging (**c**) proved the suspected diagnosis of the pulmonary sequester with a hyperintense mass in the left lower lobe (star). Nine months later, a CT angiography (**d**, **e**, **f**) was performed for planning the surgical extraction of the hyperdense lesion (arrowhead on image **e**). The CTA depicted the direct arterial supply from the thoracic aorta (arrowhead on **d**) and the venous drainage to the left lower pulmonary vein (arrowhead on image **f**).

Thoracic CT is not a first-line diagnostic tool in community-acquired and HIV-associated pneumonia. However, contrast-enhanced thoracic CT is required for the detection and differentiation of pulmonary parenchymal complications, such as empyema, abscess, bronchopleural fistula, and necrotizing pneumonia (**Figure 3**) (4). CT scanning is generally performed earlier in case of an HIV-infected child with pulmonary symptoms, since severe disease manifestations with pulmonary complications are more common.

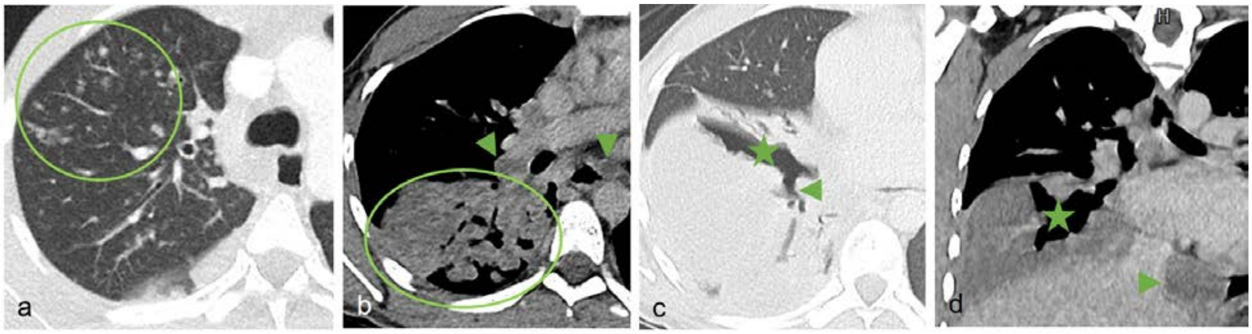

Figure 3: 17-year-old Somalian with fever and extensive pneumonia. The contrast-enhanced thoracic CT showed a “tree-in-bud” sign in several lung lobes (encircled area of the right upper lobe on image **a**) and a large hypodense consolidation in the right lower lobe with air bronchograms, consistent with necrotic liquefication (encircled area on image **b**). Peripheral enhancing lymphadenopathy is indicated with arrowheads on image **b** and **d**. An obvious connection between the bronchial tree and the consolidation is labeled with stars in image **c** and **d**; the intact segmental bronchus is marked with an arrowhead on image **c**.

Pulmonary metastases are much more common in children than primary lung malignancies. The most common sources of the pulmonary metastases are Wilms tumor, osteosarcoma, and Ewing sarcoma (5). Thoracic CT with or without contrast agent application has a higher sensitivity in the detection of the pulmonary nodules compared to chest x-ray (6) (**Figure 4**).

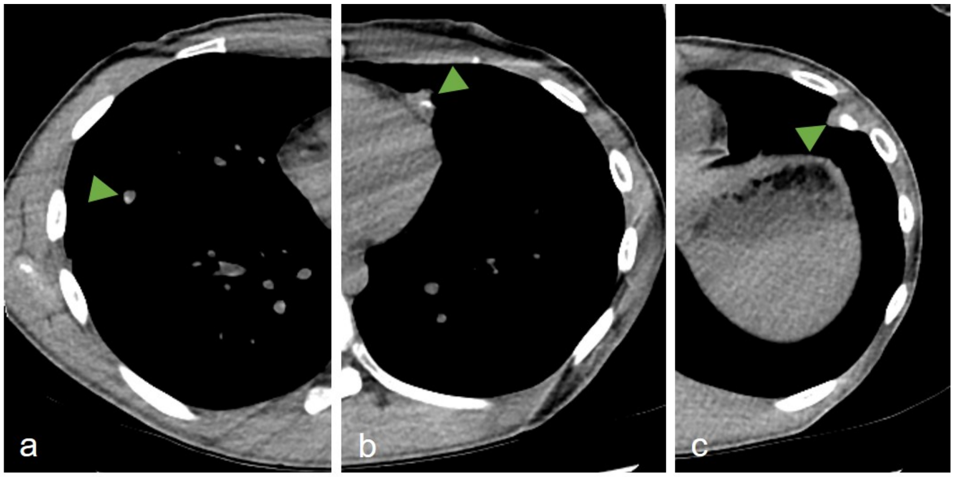

Figure 4: 14-years-old boy with known osteosarcoma. The non-contrast examination showed multiple, partial calcified lesions (arrowheads on images **a–c**) in the right upper lobe (**a**), left upper lobe (**b**), and in the inferior lingula (**c**). The findings were consistent with pulmonary metastasis.

Traumatic thoracic injuries (**Figure 5**) in children are less frequent than in adults. Blunt forces, such as motor-vehicle crashes or falls, are most commonly responsible for thoracic trauma (7). These typically result in a higher prevalence of lung contusions without any bone injuries. However, aortic and diaphragmatic injuries in children are much less frequent due to the mobility of the mediastinum (8). Thoracic CT angiography is a first-line imaging modality in traumatic cases.

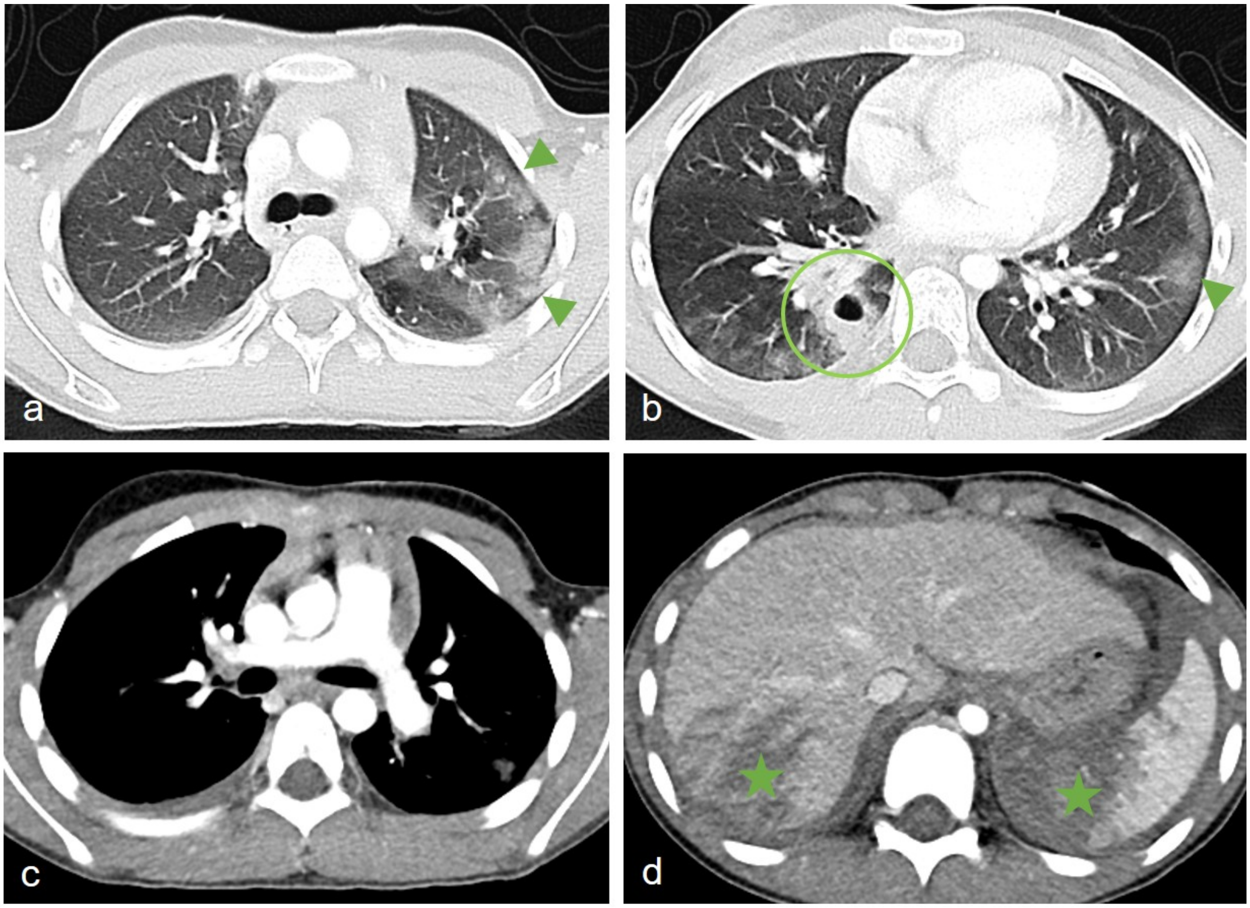

Figure 5: 11-year-old girl with chest and abdominal injury after being attacked by a cow. Contrast-enhanced CT was performed with split bolus CA application according to the polytrauma protocol. The thoracic CT showed bilateral pulmonary contusions (arrowheads on **a**, **b**) and laceration with posttraumatic pneumatocele (encircled area on image **b**). There was no sign of vascular injury on the soft tissue image (**c**). The abdominal scan demonstrated large lacerations of the liver and spleen (stars on image **d**).

Diffuse lung diseases (also called childhood interstitial lung diseases (chILD)) are rare and heterogeneous in their radiological and pathological appearance. Some of the pathologies occur predominantly in the infancy, such as congenital alveolar dysplasia, surfactant dysfunction disorders, or neuroendocrine cell hyperplasia of infancy. Other entities, such as cystic fibrosis, constrictive bronchiolitis, hypersensitivity pneumonitis, sarcoidosis, or granulomatosis with polyangiitis, might occur age-independently (**Figure 6**). Expiratory CT images are not routinely performed. In difficult cases, expiratory images are acquired as non-continuous images at three different thoracic levels (upper, middle, and lower thorax) (9).

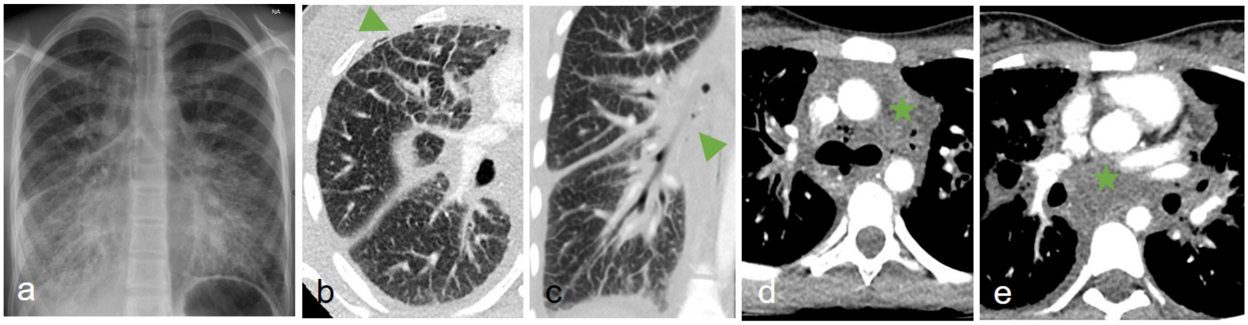

Figure 6: 14-year-old girl with dyspnea. The initial chest x-ray (**a**) presented signs of interstitial edema with Kerley lines and bilateral masking of the heart contours. Additionally, some mediastinal air stripes were detected as well. The echocardiography ruled out any cardiac disorder, and no sign of esophageal perforation was found with fluoroscopy. Afterward, the patient underwent contrast-enhanced chest CT (**b-e**), which showed bilateral thickening of the interlobular septa and some discrete mediastinal and subpleural air collection (arrowheads on panel **b** and **c**). In the soft-tissue window (**d**, **e**), significant mediastinal fluid accumulation was demonstrated (stars on panel **d** and **e**). The findings were suggestive for pulmonary lymphangiectasia, which was proven by the histology after surgical probe excision.

Children have little mediastinal fat, which results in less contrast resolution. Therefore, the acquisition of non-contrast imaging is not required, as it does not typically deliver additional information. CA application is strongly advised to evaluate any mediastinal disorders, such as in case of lymphoma in the anterior mediastinum (**Figure 7**) or neuroblastoma in the posterior mediastinum (7). The contrast-enhanced images provide valuable information on the extension of a mass as well as the infiltration of the adjacent structures. Moreover, for the evaluation of some possible complications, such as the obstruction of the superior cava vein, post-contrast images are necessary. Contrast-enhanced images are valuable in the characterization of mediastinal lymphadenopathy, as well, since the non-enhancing central necrotic lymph nodes should raise the suspicion of a prior granulomatous infection, such as tuberculosis (**Figure 3**).

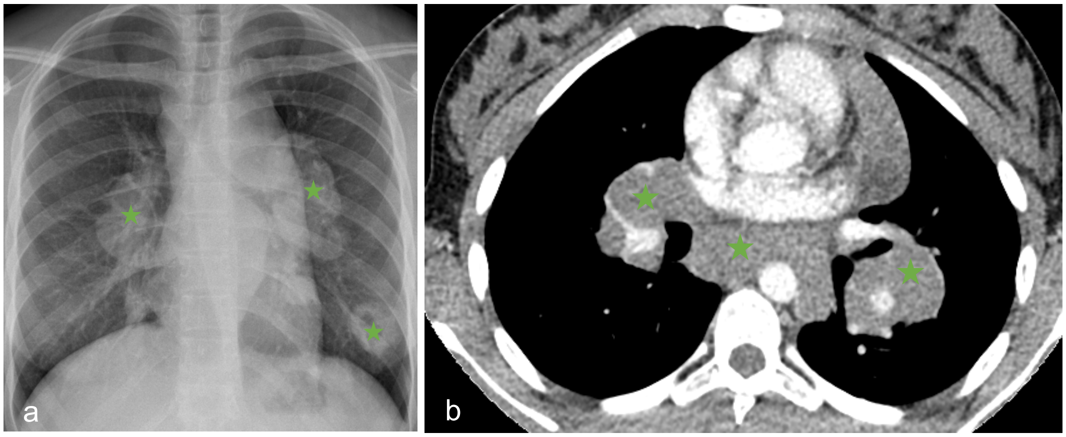

Figure 7: 13-years-old girl with dyspnea. Chest x-ray (**a**) showed huge bihilar enlargements and a pulmonary mass in the left lower lobe (stars), suggesting the diagnosis of lymphoma. Afterward, the patient underwent contrast-enhanced chest CT (**b**) with empiric delay, which verified the bihilar and mediastinal lymphadenopathy (stars).

Extracardiac vascular and cardiac disorders are more commonly evaluated with ultrasound (US) and magnetic resonance imaging (MRI), especially in small children. CT is an additional diagnostic tool in challenging cases as well as in case of preoperative planning. In case of congenital anomalies (**Figure 8**), the uniform contrast-enhancement of all vascular structures in the mediastinum is an important requirement.

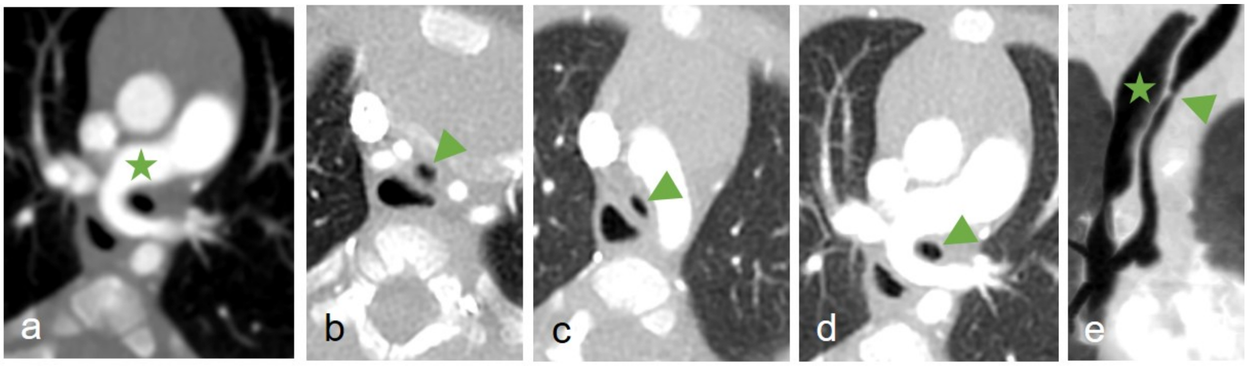

Figure 8: 4-month-old baby with VACTERL association (VACTERL stands for vertebral defects, anal atresia, cardiac defects, tracheo-esophageal fistula, renal anomalies, and limb abnormalities)**.** CTA was indicated for planning a surgical correction of a pulmonary sling (star in image **a**). Additionally, a long-segment tracheal stenosis was detected in the proximal segment of the trachea. Images **b** and **c** depict the congenital tracheal stenosis (arrowheads) at the level of the upper thoracic aperture (**b**) and aortic arch (**c**). The pulmonary sling induced a slight tracheal impression (arrowhead on image **d**). Volume-rendered

reconstruction (**e**) demonstrates the long-segment tracheal stenosis (arrowhead at the beginning of the tracheal stenosis, star in the esophagus).

Alternatively to thoracic CTA, the thoracic magnetic resonance imaging (MRI) was proved to be an appropriate diagnostic tool in several cardiothoracic abnormalities (10). In a recent comparative study between thoracic CT and MRI performed on 20 infants and neonates, the diagnostic capability of thoracic MRI were proved to be equivalent to that of thoracic CT with regard to localization and evaluation of cystic disorders, overinflation, bronchocele and solid components (11). However, the abnormal vascular connection was identified just in 57% of the cases. Moreover, due to the low spatial resolution, vascular MRI is commonly inconclusive in very young children with aortic isthmus stenosis, as indicated in **Figure 9**.

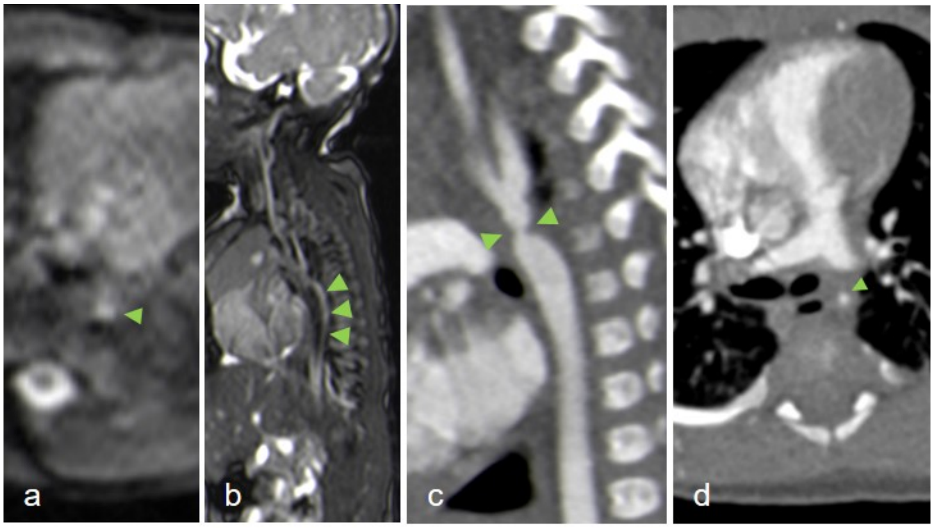

Figure 9: Two-weeks-old infant with suspected abnormalities of the pulmonary veins on the echocardiography. The first-line feed-and-wrap MRI (**a**, **b**) was able to rule out any anatomical abnormalities of the pulmonary veins. However, the aortic isthmus stenosis was apparent (arrowhead on panel **a**) with post-stenotic flow voids (arrowheads on panel **b**). Thoracic CTA (**c**, **d**) depicted the aortic isthmus stenosis with a high spatial resolution (arrowheads). Due to the impaired spatial resolution, MRI overestimated the aortic stenosis with approximately 30% in comparison with thoracic CTA.

1.2 "Children are not small adults."

CTA in small children can be challenging. Several anatomical and physiological differences between small children and adults may influence these examinations.

Firstly, young children have less bodyweight, less calcified bone structures, and a proportionally higher amount of cartilages. The relatively smaller fat content and smaller muscle mass results in secondary higher water content compared to the adults (70-75% vs. 50-60%) (12). The resulted relatively low-contrast appearance makes an adapted radiation exposure necessary for optimal image quality. This is especially important in regard to the higher amount of red bone marrow leading to a higher radiosensitivity of the developing body.

Due to the larger intravascular and extracellular fluid compartments, pediatric patients need a proportionally higher amount of CA, than the adults. The shorter CA application pathways, as well as the higher respiratory and heart rate, make the CA timing more challenging. Moreover, the tiny anatomical structures and the less mediastinal fat impede the region of interest (ROI) placement for bolus tracking.

Regarding the iodinated CA application, the renal immaturity in infants and neonates should also be considered. Immature kidneys encompass a lower renal blood flow and glomerular filtration rate (GFR) in the first two years of life as well as an immature tubular function until eight months of life.

1.3 Radiation protection in pediatric CT

CT represents a minor part of all investigations but delivers the majority of diagnostic radiation. Due to children's higher inherent radiosensitivity as well as the higher estimated risk for radiation-induced cancer (13), there is an ongoing increased awareness of the radiation protection, which has inspired several well-known campaigns, such as Image Gently, Image Wisely, AFROSAFE, EuroSafe, and Choosing Wisely in accordance with the ALARA (acronym for "As Low As Reasonably Achievable ") principle (3, 14-16).

In the last decades, diagnostic reference levels (DRL) were introduced as a dose optimization tool for each modality operating with X-rays (17). DRL represents neither an ideal dose nor an upper limit of radiation. Instead, it represents the 75% percentile of the regional or national commonly applied radiation for the purpose of orientation, but it allows a relatively wide variation in radiation dose between the individual imaging centers (18-20).

To overcome this variability and to gain a more standardized as well as optimized CT protocol, another approach with the diagnostic acceptable noise levels was proposed (17). This approach will be further discussed in chapter 1.3.2.

1.3.1 Factors influencing radiation dose

The ultimate goal of the CT imaging is to provide the best possible diagnostic information at the lowest possible dose. Notably, the best possible diagnostic image does frequently not correspond to an "aesthetically pleasing" CT image, but it is sufficient to make a proper diagnosis (21). An appropriate child-friendly environment and patient preparation with age-adapted information as well as adequate distractors, are essential to optimize an examination and to avoid unnecessary repetitions of medical imaging (22).

Several factors influence the radiation dose such as tube current, tube voltage, slice thickness and collimation, pitch, patient weight, scan length etc. (22). Of these factors, the two most important parameters are the tube voltage and the tube current. Tube voltage determines the image contrast with quadratic relation to radiation dose. The reduction of tube voltage from 120 kV to 80 kV results in an increased soft tissue and iodine contrast enabling a reduction of iodinated CA. Moreover, it is associated with a 50% more reduced radiation dose, if all other parameters are kept constant (12). Notably, the lower-energy X-rays are getting absorbed more likely in the superficial body regions than in the patient center (12). Further disadvantages of the low tube voltage technique are the increased image noise and the aggravated blooming artifacts due to metallic installations. Tube current determines the number of photons generating the image, which has a linear relationship to radiation dose as well as to image noise.

Tube current and tube voltage are determined by the size of the patient, the region of interest, the clinical question, and the contrast media, as well. The size of the patient is traditionally indexed by the body weight, although in some cases, such as obesity, the bodyweight is not reliable in assessing the patient's dimension. Notably, the bodyweight of a small and adipose child might be similar to that of a tall and thin child, but their chest dimensions are different. An individual approach for optimizing image protocol based on a cross-sectional dimension was already proposed (23), but it has not yet been implemented in the daily clinical routine.

The tube voltage is commonly adjusted to body weight (22). Imaging a region with high intrinsic contrast, such as chest and bones, justifies the reduced tube voltage, as well. To optimize the tube potential balancing between image noise and image contrast, the automatic tube voltage modulation was implemented recently (24).

The automatic exposure control (AEC) was introduced to adapt the tube current individually to patient size and the required image quality of the examination. While patient size is generally assessed by the localizer images, the determination of the necessary image quality is vendordependent; therefore, a reliable comparison between the CT scanners of different vendors is very complicated. The different vendor-specific techniques to determinate the necessary image quality, as follows:

- Siemens: reference median effective mAs (calculated as tube current x rotation time/pitch)
- GE Healthcares: noise index (defined as the noise level in the center of a water phantom on a reference scan - this definition was modified for the latest scanner versions)
- Canon: standard deviation compatible with image noise (acquired in a circular water phantom of a size of a patient

Based on the localizer images, the AEC modulates the tube current in a real-time manner in the axial plane and/or along the long axis of the patient. To avoid unnecessary radiation exposure by AEC, the patient position needs to be in the iso-center of the gentry with the arm above the head, and all unnecessary medical devices, as well as organ shield, need to be removed (25-27). The reported dose saving is variable between 15% and 50% in children (28, 29).

Further radiation dose influencing parameters are scan length and the number of acquisition phases, which are mostly influenced by the clinical question. However, the multiphase CT examinations are typically preferred to be avoided in the pediatric population. The pitch is inversely proportional to radiation exposure. However, an increased pitch above 1.5 may result in undersampling and decreased spatial resolution (30). The helical over-ranging is an important dose factor as well, which significance is growing with the increased number of acquisition channels, with the pitch, and with the wideness of collimation. Moreover, over-ranging is more substantial in the case of small children with a small scan range (30). To avoid the unnecessary radiation arising from over-ranging, adaptive collimators and low pitch need to be applied (31).

The dose optimization process in the pediatric CT frequently results in an increased image noise, which might be further reduced during post-acquisition processing. For this reason, the iterative reconstruction algorithms were introduced. The iterative reconstruction is based on complex calculations to reduce image noise while maintaining image quality (32). Therefore, iterative reconstruction allows a greater dose reduction than traditional filtered back projection reconstruction (33-35).

1.3.2 Image quality and radiation dose

There is a complicated relationship between image quality and radiation dose. Besides the spatial resolution, image quality in CT is mainly defined by the contrast resolution, which is primarily affected by image noise. Generally, image noise is determined by several factors, such as tube current, scan time, patient size, pitch factor, slice thickness, and reconstruction algorithms. More properly, the Brook's formula was created to describe the link between radiation dose and image quality, as follows:

$$D \infty \frac{B}{h \times b \times \sigma^2 \times\ a^2} \quad \text{with B = exp (μ d)}$$

- D = patient dose
- B = attenuation factor of the object
- μ = mean attenuation coefficient of the object
- d = diameter of the object
- σ = standard deviation of CT numbers (noise)
- a = sample increment
- b = sample width
- h = slice thickness

According to this equation, the dose must be doubled, if slice thickness is cut by half or if the object diameter increases by 4 cm to maintain image noise. Conversely, doubling the slice thickness will result in a 50% reduction of radiation dose for given image quality (4).

Since image quality is mainly determined by the image noise, this parameter might be an applicable reference for dose optimization, as mentioned previously (36). Assuming a fixed slice thickness according to the scanned region and clinical question, the application of an age- and size-specific clinical acceptable noise levels may result in a more harmonized and optimized radiation dose, preventing large deviations among the different pediatric centers. However, the acceptable image noise depends on the size of the patient, the examined region, the clinical question, and the experience of the reporting radiologists, as well. Therefore, the establishment of the diagnostic relevant noise levels is more complicated, although few studies have already published some reports in children, mostly on abdominal CT examinations (37-40).

1.3.3 Hidden factors of radiation exposure in the CT imaging

The imaging chain (12), which begins with the clinical referral and ends with the final CT examination, might contain some hidden factors of radiation exposure, which need to be considered, as well. First, the localizer images need to be acquired in the posterio-anterior direction with individual adjustment of the exposure parameters to the patient. This approach might save two-thirds of the scout-view dose, while protecting the radiosensitive organs, such as thyroid, breasts, and gonads (12). The second issue is the monitoring scans during bolus tracking for CTA, which might deliver a substantial amount of local radiation, as well (41, 42). Some possibilities for dose reduction in bolus tracking were already considered, but their clinical usability, especially in children, needs to be further evaluated (43-46).

1.3.4 Measures of radiation dose

The radiation dose might be described in several ways. While the dose length product (DLP) and CT dose index (CTDI) are commonly used in the adult population, none of them addresses patient size. The introduction of size-specific dose estimation (SSDE) overcomes this limitation, since SSDE handles the patient size as well, thus preventing a dose overestimation in small children and providing a better assessment of the absorbed dose (47).

1.4 Contrast agent application

For pediatric CT examinations in small children, non-ionic and iso- or low-osmotic iodinated contrast media is recommended with an osmolarity between 280 and 320 mg iodine/ml (48). However, some authors reported a CA application with 370 mg iodine/ml (49, 50) or with 400 mg iodine/ml (51) in small children, as well. In the local praxis of the Medical University of Graz, we apply a CA with 300 mg iodine/ml in infants and neonates to avoid the possible side effects due to the high osmolarity and viscosity of the CA. The CA dose is calculated according to patient weight. Due to the higher body water proportion in neonates and infants, a higher amount of CA pro body mass is commonly advised. In our local routine, the following CA dosages are applied traditionally: 2.5 ml/kg in patients younger than one year, 2 ml/kg in patients between one and two years, and 1.5 ml/kg in patients older than two years, until the maximal dosage is achieved. Notably, with the installation of the high-speed volume scanners with large detectors, the CA amount can be reduced with ca. 30% according to the local experiences. In case of a large volume (cardiac) shunt, a higher CA volume is recommended (46). To enable an easier work-up of the pediatric patients in the daily practice, local algorithms were developed, to perform unavoidable calculations for different CT examinations in children (12).

CA is generally injected through a peripheral vein flow, mostly on one of the upper extremities. However, the comparison of the different CA application sites could not show any differences in a study by Schooler et al. (50). In some special cases, like Fontan circulation, a simultaneous CA application is suggested on the upper and lower extremity to achieve a diagnostic enhancement in the main thoracic vessels, as discussed in chapter 1.4.1 (52).

Depending on the local protocols, CA might be applied manually or by a power injector. Hand application is considered to be safer in prevention the possible catheter rupture or contrast extravasation in case of a small-caliber IV catheter (50). On the contrary, mechanical CA injection is preferred by several authors, which enables a more homogenous vessel enhancement (48, 53). The injection rate needs to be adapted to the vein flow size to avoid the possible, but rare local CA extravasation (54). In both of the manual and mechanical injection, the image quality proved to be independent of the injection site (50, 55).

1.4.1 Contrast agent timing for CTA

Principally three different approaches exist on CA timing. First, the automated bolus tracking, which is based on real-time monitoring of the main bolus during a single injection. The vessel of interest is monitored continuously or intermittent by placing a ROI and with the acquisition of dynamic low-dose monitoring scans. The scanning is started manually or automatically once CA arrives into the region of interest or after a certain trigger threshold is exceeded. The applied tube voltage is set according to the following diagnostic scan to avoid contrast-to-noise differences and the consecutive inappropriate scan start. In some CT scanners, additional delay (also referred to as transit delay) may be required as well, if the monitoring level is not equivalent to the scan start level. According to the different CT scanners and the local practices, the automatic bolus tracking might be very variable among the radiological centers. If a transit delay is required before the scan start, a lower automatic bolus tracking needs to be applied.

Second, the test bolus approach, which is based on the injection of a small amount of CA (generally 15-20% of the main bolus) during the acquisition of low-dose dynamic images at the level of interest. The scan delay is calculated from the generated enhancement curves based on the density measurements. Generally, bolus tracking is preferred over the test bolus, because it delivers much homogenous vascular enhancement (56).

The application of an empirical delay is the third option for CA bolus timing, which is mostly based on the local experiences of the radiologists. The major disadvantage of this method that it neglects the individual variations in the arterial contrast arrival time in each patient. Therefore, the empirical delay is not commonly applied for angiography purposes.

1.4.2 Contrast agent application protocols

A homogenous enhancement in the arteries and veins is an important requirement for the cardiothoracic CTA in children (41). According to the clinical question and the examining center, several variable CA application protocols are suggested for this purpose (**Figure 10**). The standard dual-phase CA bolus application is widely recommended in both of the adults and pediatric patients as well, where undiluted CA is followed by a saline flush (57). For imaging congenital cardiac disorders, a triphasic protocol was suggested by Goo et al., in which the undiluted CA is followed by 50-60% diluted CA in the second phase and saline chaser in the third phase. In a modified triphasic protocol, 5-10% diluted CA is applied in the third phase instead of the saline chaser, if the visualization of the systemic veins is required (41).

Split bolus technique was proposed to achieve an adequate vascular and parenchymal enhancement in a single-phase acquisition. With this protocol, CA is applied in two phases following by saline flush in both of them, while for the second CA bolus an additional bolus tracking is performed, as well (58).

To avoid the commonly disturbing perivenous streak artifacts in the dual-phase application protocol, some authors recommend a CA application with less iodine concentration (59) or with 1:1 dilution by saline (49, 60).

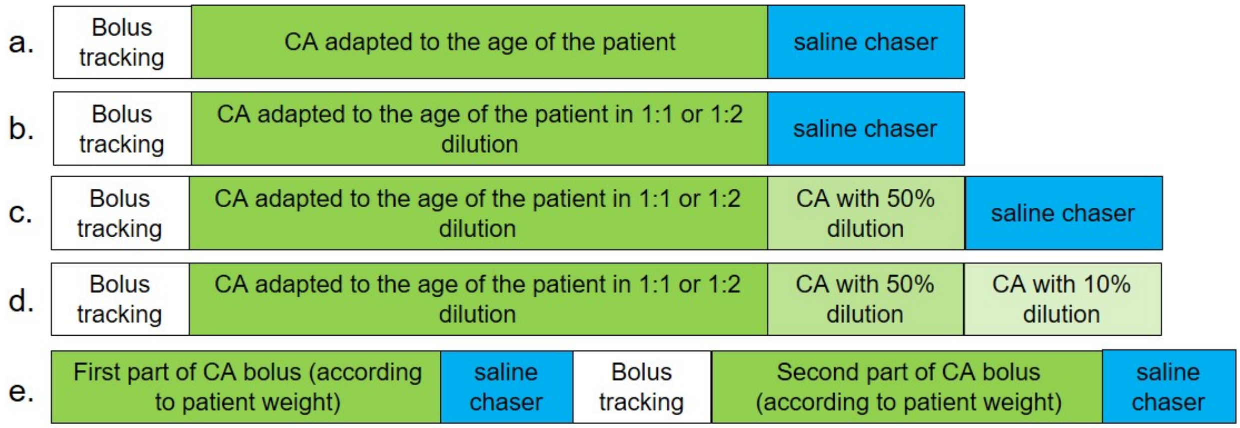

Figure 10: Schematic illustration of the different CA protocols. **a**: "conventional" dual-phase protocol, **b**: variation of the dual-phase protocol with pre-diluted CA, **c**: triphasic protocol with a saline chaser, **d**: triphasic protocol with diluted CA instead of the saline chaser to achieve a proper venous enhancement, **e**: split bolus protocol

A further variant of CA application is the institutionally developed microbolus technique (**Figure 11**) with automated bolus tracking and power injector (61). The original aim of this technique was not just to prevent the common disturbing perivenous streak artifacts, but also to optimize the CA enhancement in all major thoracic vessels in one examination. The dual-chamber power injector is programmed on the way to release 1 ml CA and 2 ml saline in the form of alternating boli. The maximum amount of CA is calculated prior to the examination according to patient weight. The CA boli are injected so long until the threshold trigger is reached (400 Hounsfield unit (HU) in descending aorta), and the scan starts automatically. At this time, the operator stops the CA application, and the rest of the CA is discharged. In comparison to the previously mentioned approach with CA dilution (49, 60), the special programmed dual-chamber power injector offers a more active control on contrast agent application by diluting the CA during the CA application, which might result in a potential reduction of the CA amount.

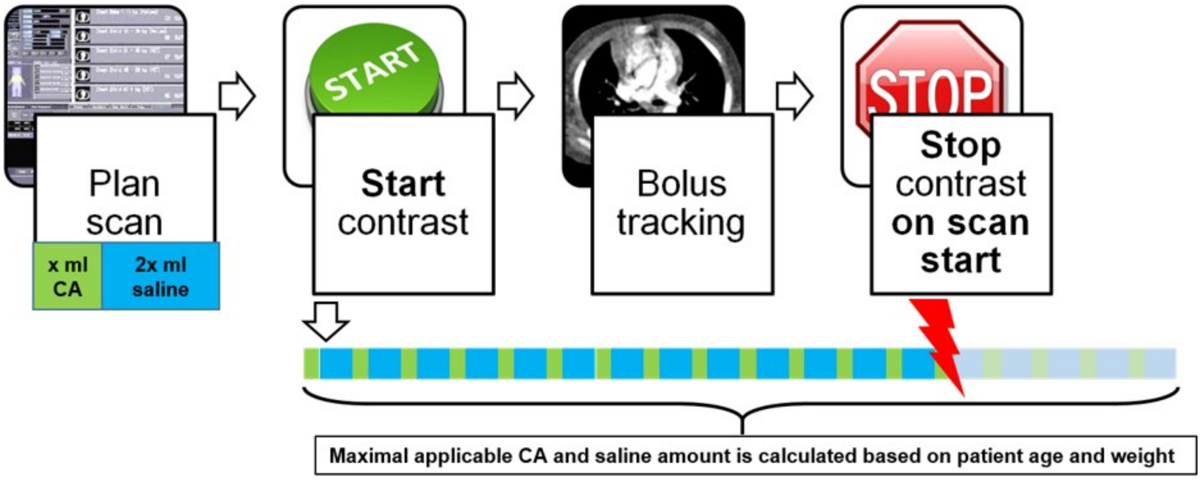

Figure 11: Schematic illustration of the MBT protocol (61).

Some special considerations are necessary in the case of univentricular palliation and Fontan circulation. Because of the higher frequency of thrombosis, especially in the heart and the central venous structures, contrast-enhanced CT is required to depict all major thoracic vessels (62). Unfortunately, the image quality of the CTA is commonly impaired by the altered anatomy and hemodynamics related to the total cavopulmonary connection, which might be further compromised by associated venous anomalies, as well (**Figure 12**). Therefore, CA is commonly applied via two catheters placed in both of the upper and lower extremity veins simultaneously (52). 60% of the CA should be injected via the lower extremity vein with a higher rate than that of the upper extremity vein. ROI should be placed in the left pulmonary artery for suspected pulmonary embolism and the aorta for suspected disorders of the pulmonary veins, aorta, or aortopulmonary collaterals. First-pass images are acquired to rule out a pulmonary embolism, and an additional delayed scan is necessary to rule out any embolism in the central vein. In some institutions, CA is applied via a single venous catheter in the upper extremity with delayed contrast timing. The contrast enhancement delay might be variable between 70 s and 3 min (62, 63). Otherwise, bolus tracking with monitoring the Fontan pathway might be successful, as well, to achieve a proper enhancement in the pulmonary arteries (64).

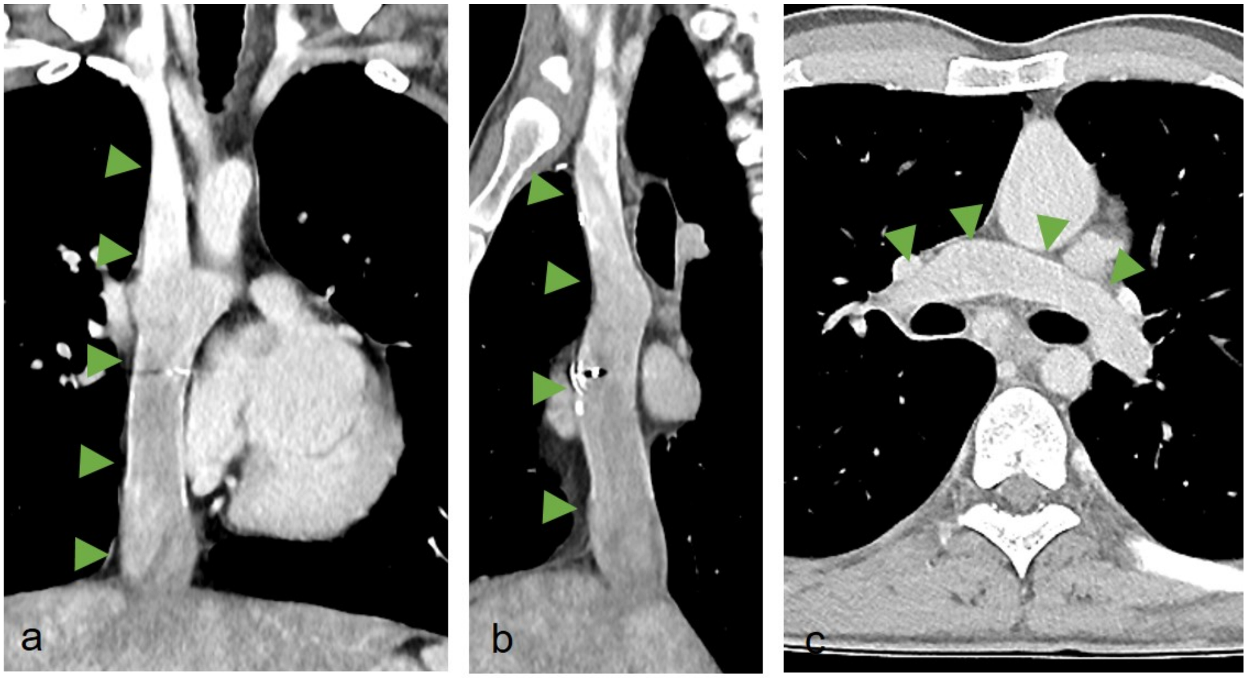

Figure 12: 21-year-old male patient with right ventricular hypoplasia and Fontan circulation. The patient was subjected to thoracic CT before implantation of a cardiac pacemaker. CA was applied through a venous line of the right upper extremity with a 50 sec delay. Images in coronal (**a**) and sagittal (**b**) plane demonstrate the mixed blood in the extracardiac Fontan channel (arrowheads on image **a** and **b**) with consecutive inhomogeneous contrast enhancement in the pulmonary trunk (arrowhead on image **c**).

1.4.3 Risks of iodinated contrast agents

The iodinated CA is a well-known and important risk factor for acute kidney injury (AKI, otherwise known as contrast-induced nephropathy). The data on AKI incidence is highly variable in the adult patient population, and some recent prospective studies have failed to show a difference in AKI incidence in patients with and without CA application (65).

The risks of iodinated CA in pediatric patients are not as well defined as in adults. Theoretically, there is an increased risk for AKI in young children due to physiological renal immaturity. However, Bedoya et al. could not prove any increase in the serum creatinine or decline in GFR after the intravenous (IV) CA application in patients younger than one month (66). Even in neonates after neonatal cardiac surgery, the CA application was not followed by an increased risk for AKI (67).

In a retrospective study with the inclusion of 867 patients (<18 years), the authors compared patients who underwent native and contrast-enhanced CT (68). In the primary cohort analysis, the incidence of AKI was 3.3% in the contrast group and 0.1% in the native group. After propensity score adjustment, the authors could not show any difference regarding the AKI incidence between the two matched groups (305 patients in both groups with a median age of 14 and 15 years).

In a single-center retrospective study, Cantais et al. could show an AKI-incidence of 10.3% in 233 included pediatric patients after CA application (median age of 5.9 years, IQR 1.9-13.7 years). However, no control group was included in the analysis in this study (69).

Besides the renal side effects, the osmolarity of CA has particular importance in neonates and small children. The smaller and younger is the child, the more susceptible they are to fluid shifts and have a lower tolerance for intravascular osmotic loads in comparison to the adults. As previously mentioned, low-osmolar CA is approved in pediatric patients with an iodine concentration of 300 – 350 mg iodine/ml or less. Although these CAs are considered low-osmolar, their osmolarity (521 ± 24 mOsm/kg and 618 ± 29 mOsm/kg, respectively) is high above full-blood osmolarity (275 to 295 mOsm/kg). Each iodinated CA has a higher viscosity than blood, and with the increasing iodine concentration, the CA viscosity is increasing, as well. The CA with 300 mg iodine/ml has a viscosity of 4,5±4 kPa.s,37 ℃, while with 350 mg iodine/ml of 7,5 ± 0,6 kPa.s,37 ℃. As the viscosity of CA is temperature-dependent; therefore, CA is routinely pre-warmed before the injection to avoid the local side effects (70).

The frightening allergic reaction after the CA application might happen in pediatric patients as well. Its incidence (0.18 % to 0.46 %) is, however, much lower than that of adults (71).

Besides the traditional risk factors of the CA application, a newer side-effect has gained more attendance, which is related to radiation-induced deoxyribonucleic acid (DNA) damage. The correlation between the amount of the radiation-induced DNA damage and the DNA double strand-breaks is well-known, which might play an important role in the carcinogenesis unless they get repaired or paired (72). Recent studies pointed out that the application of the iodinated CA increases the frequency of the harmful double strand-breaks (73, 74). Wang et al. analyzed DNA double-strand breaks of peripheral lymphocytes in altogether 70 patients who underwent unenhanced or enhanced abdominal CT (75). The results showed a 90% increase in DNA double-strand breaks in patients who received the CA application before the CT examination compared to the patients who underwent native CT or received CA after the irradiation. Moreover, animal experiments on minipigs demonstrated that the amount of DNA double-strand breaks depends on the applied iodine load (76). Despite these findings, the individual biological damage is hard to assess because of its dependency on several other factors, such as individual radiation sensitivity or repair capacity (72).

1.5 Risks of anesthesia

Anesthesia is commonly in charge of the pediatric radiology departments due to the requirement of a motion-free radiological examination in small and/or disabled children. The short-term risks of the anesthesia are well-known, but recently the long-term risk of neurodevelopmental impairment raised concern. Initially, a relationship between the administration of general anesthetics during the period of the rapid brain growth and an increase of neuronal apoptosis, as well as a neurocognitive impairment, was observed in animal studies (77). Although the general risk of neurodevelopmental impairment is hard to quantify, several retrospective and prospective studies examined this issue (78-81). For example, Wang et al. stated that there is a modestly elevated risk of adverse neurodevelopment in children who were exposed to anesthesia during early childhood (before four years of age), especially if the exposure was repeated (82). Based on the findings, the FDA (U.S. Food and Drug Administration) gave out a warning on anesthetic medications in young children and pregnant women (83). According to this document, an "exposure to these medicines for lengthy periods of time or over multiple surgeries may negatively affect the brain development in children younger than three years". Additionally, animal studies proved nerve cell damage in the developing brain after exposure to general anesthetics or sedation over three hours, which might result in long-term adverse effects on the animal's behavior or learning. However, in a recently published international multicentre randomized-controlled study, the authors compared patients who underwent herniorrhaphy in the early infancy under general anesthesia with a volatile anesthetic or awake-regional technique (84). The authors concluded that a short length general anesthesia (less than one hour) in early infancy does not influence the neurodevelopmental outcome at the age of five years.

Still, the emerging concerns about the administration of anesthetics induced more intensive research to avoid the anesthesia in the CT, as well. As a possible solution to this issue, fast dual-source CT imaging was introduced with high pitch mode (85, 86). Kim et al. compared thoracic CT imaging on a dual-source CT with high pitch "Flash spiral" mode and low pitch "X-CARE" mode in young children (mean age 35.6 months) (87). According to their results, the high pitch mode proved to be efficient in diminishing motion artifacts resulting in better image quality. However, due to the z-overscanning effect, the high-pitch CT examinations tend to result in higher radiation doses in young patients despite the applied adaptive dynamic collimation.

Kino et al. examined the possibility of anesthesia-free thoracic imaging with ultrafast CT on patients younger than three years (88). The research group included 101 children with and without anesthesia, who underwent a chest CT examination on a dual-source high-pitch (1.95 – 3.0) CT with a gantry rotation of 0.28 s. The image quality of these ultrafast scans was analyzed. The authors concluded that the examinations with anesthesia were significantly less impaired by motion artifacts, which resulted in better overall image quality. However, the examinations without anesthesia proved to be sufficient for the diagnosis, as well. The sub-group analysis of motion artifacts on cases with and without CA (CA application in 71% of the patients with general anesthesia and 22% of the patients without anesthesia) revealed no significant difference. However, the relatively large difference between the incidences of CA application in the subgroups may limit this result.

2. Goal of this dissertation

As it was addressed in the previous chapters, pediatric CT angiography is still a complex and challenging task for radiologists. This dissertation was dedicated to examining some unique aspects of pediatric thoracic CT angiography.

First, a phantom study was designed to provide calculations on threshold optimization for the bolus tracking technique. The examinations were conducted on three different CT scanners to achieve comprehensive data with every possible tube voltages, and the potential differences, as well as their clinical relevance, are going to be discussed, as well.

Second, a single-center retrospective study was conducted with the hypothesis that in the chapter 1.4.2 introduced microbolus protocol delivers higher image quality with less contrast agent amount.

3. Materials and Methods

The doctoral candidate conducted a phantom analysis on an Electron Density Phantom with different tissue-mimicking contents as well as assessed pediatric thoracic CTs with different CA application protocols in infants and neonates in a single-center retrospective study.

3.1 Ethics approval, conflict of interest statement

For the phantom study no institutional review board approval was required.

The Ethics Committee of the Medical University of Graz approved the study protocol on pediatric patients, the approval number EK 29-390ex16/17. Due to the retrospective character of the study, no written informed consent was required from the parents/guardians of the study participants.

The doctoral candidate declares that the research was conducted in the absence of any commercial or financial relationship that could bias the results presented. The doctoral candidate declares no conflict of interest.

3.2 Phantom

Measurements were conducted on an Electron Density Phantom (Model RMI 467, Gammex Inc., Middleton, WI). This phantom contains 16 insert chambers in a 33 cm wide and 5 cm high Zero HU Solid Water® disk **(Figure 13)**. As listed in **Table 2**, 13 different materials were filled in the 16 chambers of the Electron Density Phantom. The physical densities ranged from 0.30 to 1.82 g/cm^3. Four individual chambers contained solid water filling with 1.02 g/cm^3 physical density, although one chamber had to be ruled out from the final analysis due to artificial air content and consecutive deviation of the density measurements.

Similarly to the study of Sande et al. (89), chambers were divided into two groups:

1. physical densities far from that of true water (1.00 g/cm^3) with lung and bone chambers (0.3 - 0.45 g/cm3 and 1.12 - 1.86 g/cm^3, respectively)
2. physical densities close to that of true water (1.00 g/cm^3) with soft tissue and solid water chambers (0.92 – 1.08 g/cm^3)

Figure 13: Electron Density Phantom. The photo documentation on the right side, CT image of the same phantom on the left side with labeled chambers (on the left image, numbers indicate the physical density in g/cm3).

Tissue Mimicking Inserts	*Electron density relative to water*	*Physical density (g/cm^3)*
Lung (LN-300)	0.29	0.30
Lung (LN-450)	0.40	0.45
Adipose (AP6)	0.90	0.92
Breast	0.96	0.99
Zero Solid Water	0.99	1.02
Brain	1.05	1.05
Liver (LV1)	1.07	1.08
Inner Bone	1.09	1.12
Bone (B200)	1.11	1.15
Bone (CB2-30% Mineral)	1.28	1.34
Bone (CB2-50% Mineral)	1.47	1.56
Cortical Bone (SB3)	1.69	1.82
True Water	1.00	1.00

Table 2: 13 different tissue-mimicking insert in the Electron Density Phantom.

3.3 Patients

The procedure of patient selection is depicted in **Figure 14**. Our institution (Division of Pediatric Radiology of the Department of Radiology at the Medical University of Graz) performed 1591 thoracic CT examinations between 2007 and 2017. From 1591 thoracic CTs we considered only those where CA was applied and were performed on patients younger than 24 months (n=112). An additional 42 examinations were ruled out where iodine concentration exceeded the 300 mg iodine/ml, or the tube voltage was higher than 80 kV. Altogether 70 examinations from 58 unique sequential patients met the eligibility criteria. In 9 patients, the clinicians asked for repeated CT examinations. Repeated examinations were handled separately since the circulatory and heart condition of a patient is more determining for the CT investigation than the final diagnosis.

Furthermore, the cardiovascular status of patients can show certain variability at the specific moment of the CT examination. Examinations were divided into three groups according to the applied CA application protocol, as depicted in **Figure 14**. CA was administered in 32 CT scans according to MBT protocol, in 23 scans according to "conventional" thoracic angiography with biphasic protocol, and in 15 scans with (empirical) fixed bolus delay. The age and weight of the examined patients were available from the medical records. To get an accurate picture of the patient's body dimension, the doctoral candidate calculated the effective diameter manually according to (47). The primary diseases of patients were characterized according to consensus international guidelines (1).

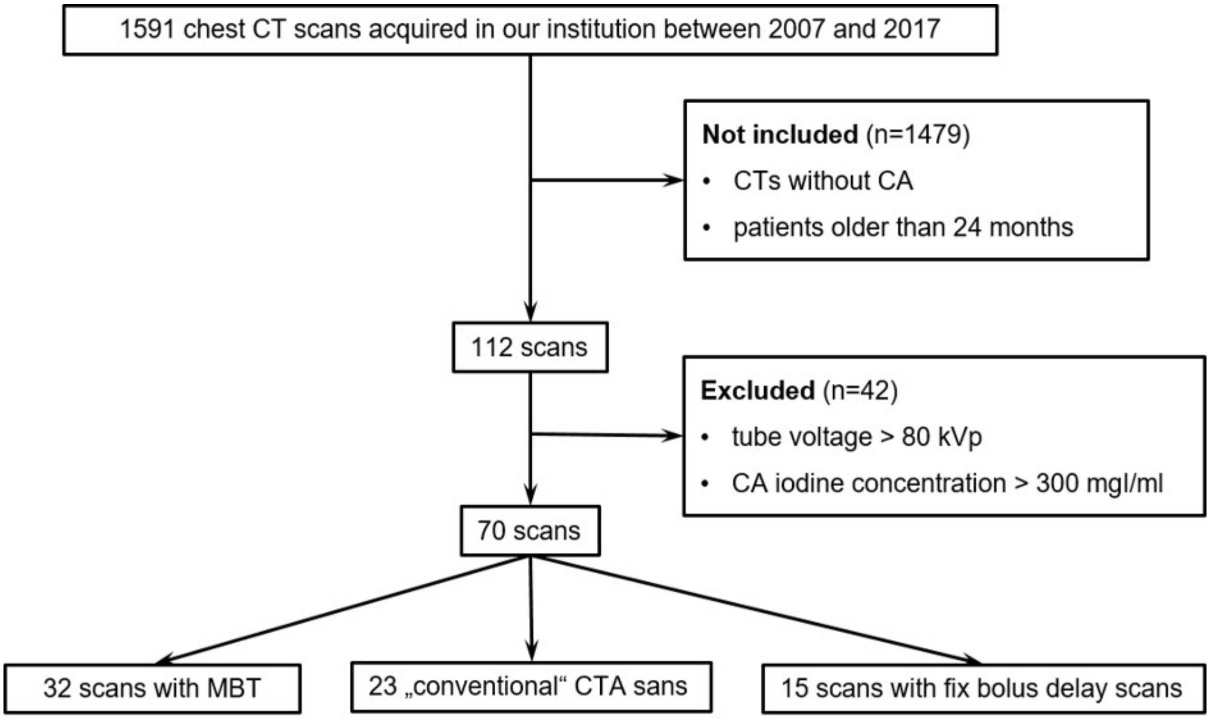

Figure 14: Flow chart of study population (61).

3.4 Image acquisition

3.4.1 Phantom scanning settings

Radiographers performed the CT examinations on three different CT scanners at the Department of Radiology of the Medical University of Graz. Firstly, on a 320-slice Aquilion One volume scanner (Canon Medical Systems, Tokyo, Japan), which has been in use at the Division for Pediatric Radiology since 2007. The most striking feature of this scanner is the wide detector, which enables to cover a maximum scan range of 16 cm per single tube rotation (90). Secondly, on a third-generation dual-source SOMATOM Force (Siemens Medical Solutions, Erlangen, Germany) scanner with Vectron x-ray tube and Stellar Infinity detector (91) installed in 2018. Last but not least, on a 256-slice dual-source volume scanner (Revolution, GE Medical Systems, Milwaukee WI, USA), which was installed in 2019. These scanners are used in the daily routine undergoing regular quality controls according to the local regulations. Despite the several hardware and software differences between the CT scanners, scanning protocols were as standardized as possible. Dual-source scanners were applied in single-source mode. Each scan was conducted with every available tube voltage on a particular CT machine, which were (in kV)

80, 100, 120 and 135 for Aquilion ONE; 70, 80, 90, 100, 110, 120, 130 and 140 for SOMATOM Force and 70, 80, 100, 120, 140 for Revolution, respectively (**Table 3**). The automatic exposure control was inactive in all of the examinations. To achieve more standardization among the scan protocols and to minimize image noise possible, tube current was set in a way to gain the possible highest radiation dose at a given tube voltage. Images were reconstructed with a 3 mm slice thickness. **Table 3** summarizes all three exposure protocols.

	Tube voltage (kV)	**Tube current (mA)**	**Slice thickness (mm)**	**CTDIvol (mGy)**	**DLP (mGy.cm)**	**Exposure (mAs)**	**Exposure time (msec)**	**Filter**	**Kernel**
Aquilion ONE	80	500	3	12,4	220,3	375	750	LARGE	FC18
	100	500	3	25,4	450,3	375	750	LARGE	FC18
	120	500	3	41,7	738,4	375	750	LARGE	FC18
	135	200	3	57,6	1020,1	375	750	LARGE	FC18
SOMATOM Force	70	700	3	11,69	169,2	1000	1000	FLAT	Bv36s\3
	80	588	3	16,11	233,2	840	1000	FLAT	Bv36s\3
	90	467	3	19,23	278,2	666	1000	FLAT	Bv36s\3
	100	378	3	21,55	311,9	540	1000	FLAT	Bv36s\3
	110	313	3	23,28	336,9	446	1000	FLAT	Bv36s\3
	120	263	3	25,03	362,3	375	1000	FLAT	Bv36s\3
	130	224	3	26,03	376,7	319	1000	FLAT	Bv36s\3
	140	193	3	26,62	385,3	275	1000	FLAT	Bv36s\3
Revolution	70	500	3	6,50	67,96	12	1000	BODY	STANDARD
	80	500	3	10,37	103,66	12	1000	BODY	STANDARD
	100	720	3	29,27	292,67	18	1000	BODY	STANDARD
	120	740	3	48,5	485,01	18	1000	BODY	STANDARD
	140	635	3	60,58	605,85	15	1000	BODY	STANDARD

Table 3: Scanning protocol of the Electron Density Phantom on three different CT scanners.

3.4.2 Patient scanning settings

In the course of the retrospective analysis (61) all patients were scanned with the previously described Aquilion One CT scanner (Toshiba Medical Systems Corporation, Otawara-shi, Japan) at the Division of Pediatric Radiology of Medical University of Graz.

The automatic exposure control (AEC) was regularly active. None of the examinations were conducted with electrocardiographic gating. Helical and volume scans were conducted. Since the machine update in 2012, adaptive iterative reconstruction (AIDR) was activated, as well. Based on the clinical question, the responsible radiologist decided the slice thickness of the reconstructed images in soft tissue and lung kernels. Images were reconstructed with a 50% increment of slice thickness. The reconstruction kernels were variable, according to the actual technical setup of the CT scanner. **Table 12** summarizes the technical parameters. Patients received sedation during every CT scans by an anesthetist in charge.

3.4.3 Contrast agent application protocol

In all groups, the contrast agent was calculated prior to the CT examination based on patient weight (12). Patients in group I (n=32) received CA according to the so-called "microbolus technique" developed in our institution (61), while in group II (n=23) according to the standard dual-phase protocol. Automatic bolus tracking was performed in group I and II, where the ROI was placed in the descendent aorta to prevent the excessive table movement prior to the CT scan. The automatic bolus tracking threshold was set at 400 HU in both of these groups. In the third group (n=15), CA was injected with a fixed empirical bolus delay. CA was administrated by the same power injector (Ulrich GmbH&Co.KG, Ulm, Germany) in all groups.

3.5 Image analysis

3.5.1 Phantom images

Densities in HU were measured with syngo.plaza© software package (Siemens Healthcare GmbH, Erlangen, Germany) in each image set by setting a 4 cm^2 ROI on the central slices of each chamber. The revealed mean HU represented the characteristic HU value, while the standard deviation of HU represented image noise for that of a particular chamber. Individual ROI measurements were conducted three times. The mean values were considered as characteristic and were recorded in an Excel spreadsheet (Microsoft, Redmond, United States of America). The doctoral candidate was allowed to adapt the window settings during the image analysis.

3.5.2 Assessment of contrast enhancement in pediatric thoracic CTs

An objective and subjective analysis was performed. As objective image analysis, quantitative mean contrast enhancement was measured by placing a circular ROI in several anatomical localisations, as follows: ascending aorta (AA), aortic arch (Aar), descending thoracic aorta (AD), pulmonary trunk (PT), all heart chambers (RA for right atrium, LA for the left atrium, RV for the right ventricle, LV for the left ventricle), all four pulmonary veins close to their origin (RUPV for the right upper pulmonary vein, RLPV for the right lower pulmonary vein, LUPV for the left upper pulmonary vein, LLPV for the left lower pulmonary vein), superior vena cava (SCV), liver (Li) and para-spinal as well as pectoral muscles (Mu) (**Figure 15**).

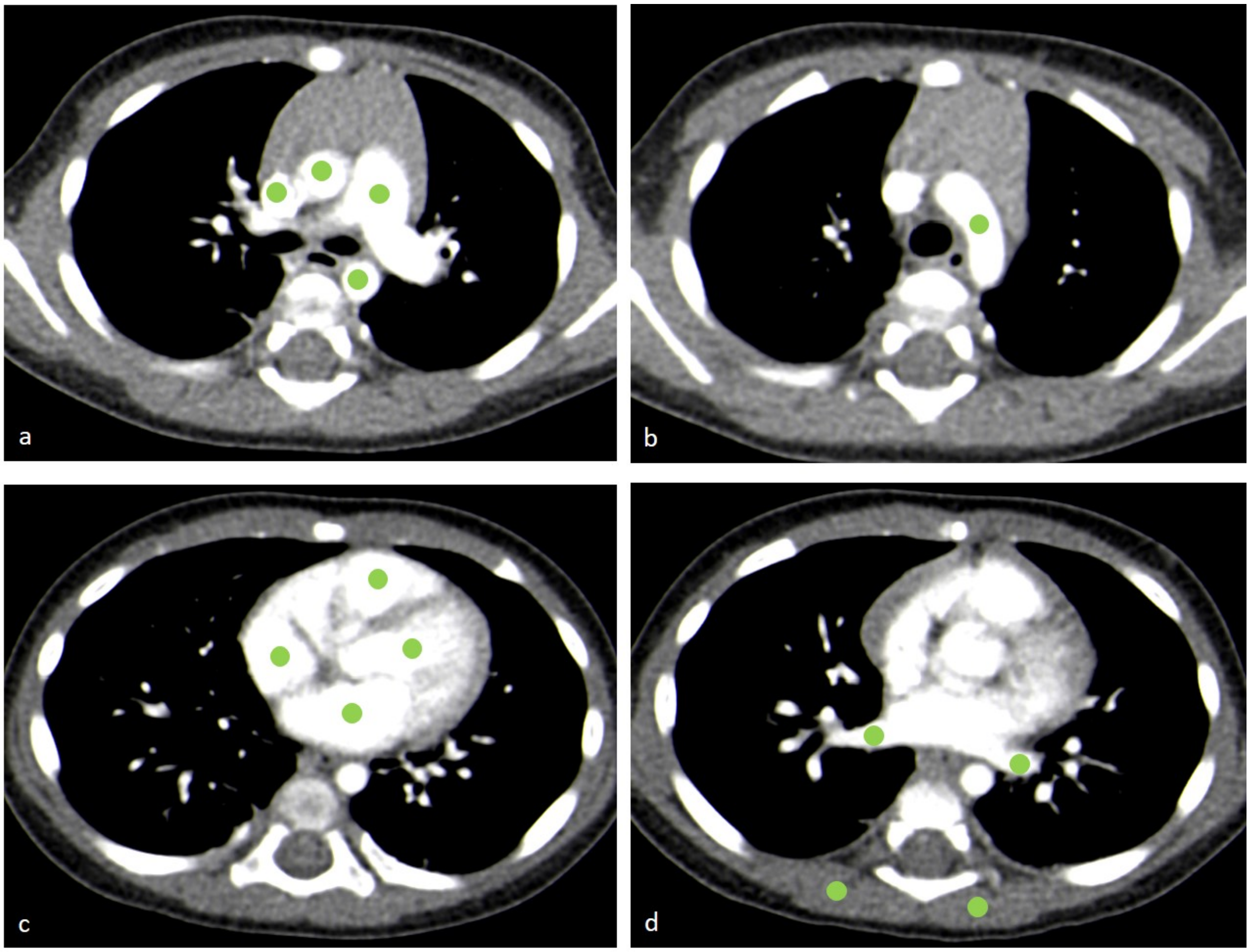

Figure 15: Representative CT images in the axial plane to demonstrate the locations of the objective image analysis with green circles. The ROI measurements were performed in the following localisations (from left to right): superior cava vein, ascending aorta, descending aorta, pulmonary trunk on panel **a;** aortic arch on panel **b**; right atrium, left atrium, right ventricle and left ventricle on panel **c**; right paravertebral muscle, right lower pulmonary vein, left paravertebral muscle, left lower pulmonary vein on panel **d.**

ROI measurements were repeated three times, and the mean and standard deviation of attenuation coefficients (HU) were recorded, and the mean HU values were computed afterward.

This value represented the characteristic mean enhancement, while the standard deviation corresponded to the image noise for that particular area. Signal-to-noise (SNR) and contrast-to-noise ratios (CNR) were computed using the following formulas (92, 93):

$$\mathrm{SNR} = \frac{\text{mean peak enhancement}}{\text{standard deviation of the mean peak enhancement of a given region}}$$

$$\mathrm{CNR} = \frac{\text{mean peak enhancement of that region} - \text{mean peak muscle enhancement}}{\text{image noise measured in muscle regions}}$$

To assess the general homogeneity of contrast enhancement in one group, the mean vascular enhancement of the different regions in each group were compared, respectively.

3.5.3 Subjective image quality analysis of the thoracic CTs

The doctoral candidate and another pediatric radiologist with eight years of professional experience (S.T.) rated the image quality and CA-related image artifacts in consensus. The general image quality was scored on a five-grade Likert scale as follows: score 1 for "excellent", score 2 for "good", score 3 for "acceptable", score 4 for "poor", and score 5 for "bad". In the general image quality assessment, observers considered all kinds of image artifacts (94) including CA-related artifact, motion artifacts as well as beam hardening artifact due to device in scan field, and image noise. Artifacts related to contrast enhancement were analyzed separately on a four-grade Likert scale as follows: score 1 for "no artifacts", score 2 for "minor artifacts", score 3 for "significant artifacts", and score 4 for "excessive artifacts" with marked image blurring. **Figure 16** demonstrates the four-grade Likert scale for image artifact analysis with four example images. The observers reviewed the CT studies in a dark reading room on calibrated four-megapixel RadiForce RX440 monitors (Eizo, Hakusan, Japan) with the local PACS software, syngo.plaza VB20A (Siemens Healthineers, Erlangen, Germany). Individual adaption of center and windows settings was allowed for the observers.

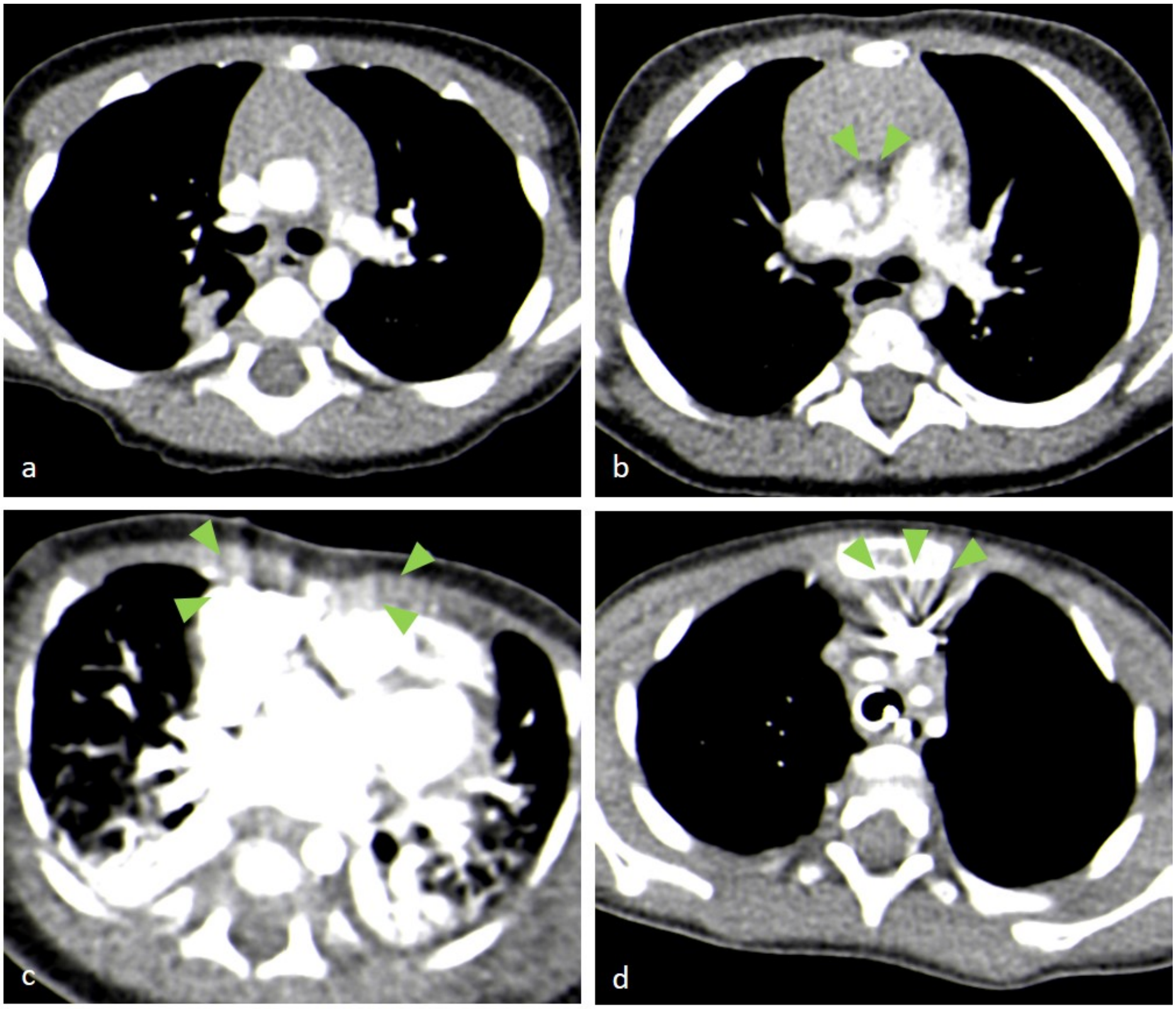

Figure 16: Illustration of the four subjective categories of CA-related image artifact assessment. a: no image artifacts, **b**: minor image artifacts (green arrowheads), **c**: major/significant image artifacts (green arrowheads), **d**: excessive image blurring due to marked image artifacts (green arrowheads) [adapted and modified after (61)].

3.6 ABT threshold calculations

ABT threshold calculations were performed to identify the compatible HU threshold values at different tube voltages. Detailed literature research preceded the threshold calculations, which revealed several widely variable threshold values between 70 HU and 400 HU (50, 55, 60, 61, 93, 95, 96). Despite in-depth literature screening, no data was found regarding the tube voltage, at which the published variable ABT thresholds were defined. Therefore, it was assumed that the

ABT threshold values were defined empirically at 120 kV, and a wide range of potentially useful reference thresholds (200 HU, 150 HU, 120 HU, 100 HU, 90 HU, 80 HU, 70 HU) were defined at 120kV for the analysis.

The adjusted thresholds were calculated in three steps. As a first step, physical densities were determined for all reference thresholds and on each scanner, respectively. For this purpose, curve fitting was performed with linear regression between the phantom's physical densities and the measured HU values at a tube setting of 120 kV. **Table 4** demonstrates the obtained linear equations and physical densities.

			Aquilion ONE	SOMATOM Force	Revolution
Linear equation			y=0.97+8.21E-4*x (r^2=0.956)	y=0.96+7.87E-4*x (r^2=0.956)	y=0.97+7.84E-4*x (r^2=0.952)
Reference physical density (g/cm^3)	Reference threshold (120 kV)	200 HU	1.133832	1.120967	1.13110600
		150 HU	1.092782	1.081617	1.09190600
		120 HU	1.068152	1.058007	1.06838600
		100 HU	1.051732	1.042267	1.05270600
		90 HU	1.043522	1.034397	1.04486600
		80 HU	1.035312	1.026527	1.03702600
		70 HU	1.027102	1.018657	1.02918600

Table 4: Linear equations and the calculated reference physical densities for each scanner, respectively. In the equation forms E-4 for 10^{-4} and E+4 for 10^{4}.

As a second step, a second curve fitting was conducted at all available kV settings and for every CT scanner to estimate the HU values by the previously established physical densities. As indicated in **Table 3**, on each CT scanner only a particular set of kV was applicable, which were (in kV) 80, 100, 120 and 135 for Aquilion ONE; 70, 80, 90, 100, 110, 120, 130 and 140 for SOMATOM Force and 70, 80, 100, 120, 140 for Revolution, respectively. Each resulted HU value represents the ABT threshold for a given kV setting in a particular CT scanner.

As a third step, ABT thresholds for everyday use were obtained by averaging the ABT thresholds of similar kV settings.

3.7 Statistical analysis

3.7.1 Comparison of measured density values of Electron Density Phantom

Mean density values at tube voltages available on all three scanners (80, 100, and 120 kV) were compared with one-way ANOVA, while at tube voltages feasible on the Siemens and GE scanners (70 kV and 140 kV) with paired t-test.

Bland-Altman analysis with subsequent linear regressions was conducted to rule out any systemic bias between two scanners (97).

For statistical analysis, current versions of SPSS Statistics (IBM Corp., Armonk, NY) and GraphPad Prism (GraphPad Software, La Jolla California USA) software were used.

3.7.2 Statistical analysis of enhancement in thoracic CTA

The collected patient's data were analyzed in SPSS Statistics version 21 (IBM, New York, United States of America) as well as in SAS® software version 9.4 (SAS Institute, Cary, NC, USA). Data were expressed as mean and standard deviation or median and 95% confidence intervals unless otherwise stated. Linear models with adjustment to the patient's age and weight were applied for comparison of contrast enhancement between the groups. ANOVA tests were conducted to analyze the homogeneity of mean enhancement between the different vascular structures in every group, respectively. Scaled subjective image quality (see also chapter 3.5.3) between groups were compared with Fischer's exact test. The significance level was set to α=0.05.

4. Results

4.1 Phantom study

4.1.1 Threshold quantification based on phantom density measurements

ABT thresholds at different tube voltages are demonstrated in **Table 5** for each respective CT scanner. **Figure 17** and **Table 6** summarize the mean ABT thresholds. The highest standard deviations in ABT thresholds were found at 80 kV (± 10 HU).

	kV	Linear equation for threshold calculation	r^2	Reference threshold HU values at 120 kV						
				200 HU	150 HU	120 HU	100 HU	90 HU	80 HU	70 HU
Aquilion ONE	80	y=-1.28E3+1.38E3*x	0.906	288.7	232.0	198.0	175.4	164.1	152.7	141.4
	100	y=-1.17E3+1.23E3*x	0.947	224.8	174.3	144.1	123.8	113.8	103.7	93.6
	120	y=-1.13E3+1.17E3*x	0.956	195.9	148.1	119.4	100.3	90.7	81.1	71.6
	135	y=-1.07E3+1.11E3*x	0.963	181.1	135.6	108.4	90.2	81.1	72.1	64.0
SOMATOM Force	70	y=-1.47E3+1.59E3*x	0.894	313.0	250.4	212.8	187.7	175.2	162.6	150.1
	80	y=-1.37E3+1.47E3*x	0.918	273.7	215.9	181.3	158.2	146.6	135.1	123.5
	90	y=-1.29E3+1.37E3*x	0.932	242.9	189.0	156.7	135.2	124.4	113.7	102.9
	100	y=-1.25E3+1.31E3*x	0.943	224.6	172.9	141.9	121.3	111.0	100.7	90.4
	110	y=-1.21E3+1.26E3*x	0.950	210.2	160.5	130.7	110.9	100.9	90.9	81.9
	120	y=-1.17E3+1.22E3*x	0.956	196.4	148.6	119.9	100.7	91.2	81.6	72.1
	130	y=-1.13E3+1.17E3*x	0.961	181.7	135.5	107.8	89.3	80.2	70.9	61.7
	140	y=-1.11E3+1.14E3*x	0.964	176.2	131.1	104.1	86.1	77.0	68.0	59.0
Revolution	70	y=-1.45E3+1.56E3*x	0.890	310.2	249.1	212.5	188.0	175.8	163.6	151.4
	80	y=-1.36E3+1.45E3*x	0.915	270.9	214.3	180.3	157.6	146.3	134.9	123.6
	100	y=-1.25E3+1.3E3*x	0.940	223.3	172.4	141.8	121.5	111.3	101.1	90.9
	120	y=-1.18E3+1.21E3*x	0.952	195.3	147.7	119.2	100.2	90.6	81.1	71.6
	140	y=-1.15E3+1.17E3*x	0.961	176.2	130.1	102.5	84.1	74.8	65.6	56.4

Table 5: Calculated threshold values at different voltages on three different scanners

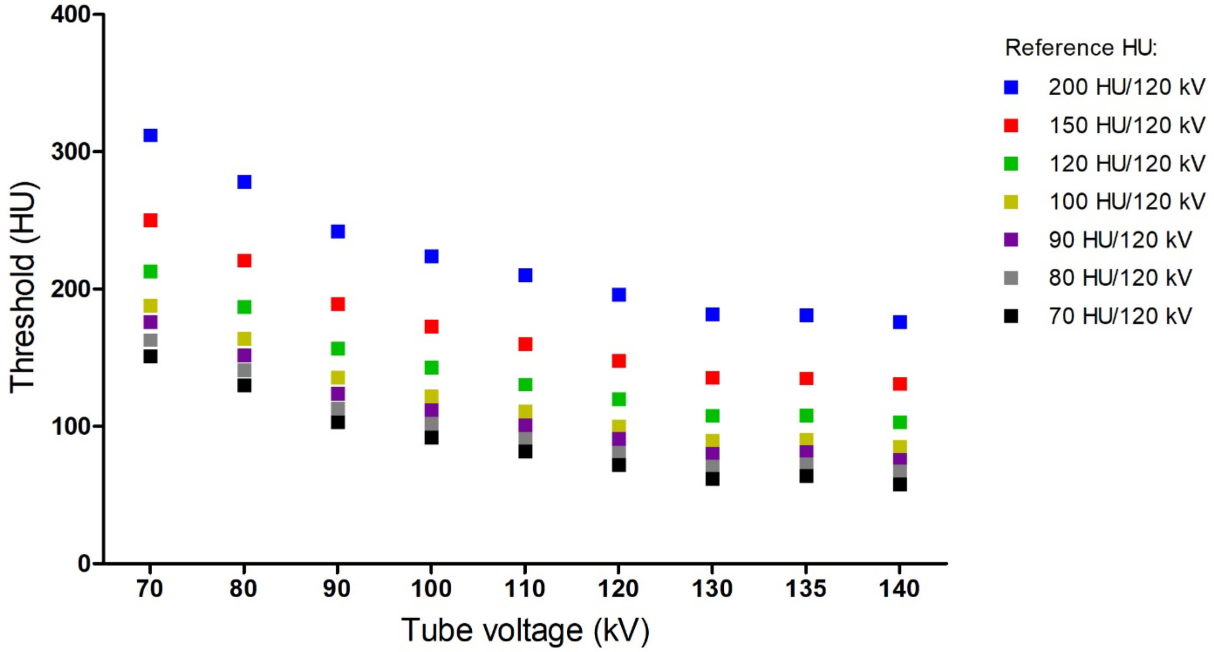

Figure 17: Scatter plot illustrating computed threshold values for different reference thresholds at different tube voltages.

	Reference threshold HU values at 120 kV						
	200 HU	**150 HU**	**120 HU**	**100 HU**	**90 HU**	**80 HU**	**70 HU**
70 kV (n=2)	312 ± 2	250 ± 1	213 ± 0	188 ± 0	176 ± 0	163 ± 1	151 ± 1
80 kV (n=3)	278 ± 10	221 ± 10	187 ± 10	164 ± 10	152 ± 10	141 ± 10	130 ± 10
90 kV (n=1)	242.9	189.0	156.7	135.2	124.4	113.7	102.9
100 kV (n=3)	224 ± 1	173 ± 1	143 ± 1	122 ± 1	112 ± 2	102 ± 2	92 ± 2
110 kV (n=1)	210.2	160.5	130.7	110.9	100.9	90.9	81.9
120 kV (n=3)	196 ± 1	148 ± 0	120 ± 0	100 ± 0	91 ± 0	81 ± 0	72 ± 0
130 kV (n=1)	181.7	135.5	107.8	89.3	80.2	70.9	61.7
135 kV (n=1)	181.1	135.6	108.4	90.2	81.1	72.1	64.0
140 kV (n=2)	176 ± 0	131 ± 1	103 ± 1	85 ± 1	76 ± 2	67 ± 2	58 ± 2

Table 6: ABT thresholds after averaging the calculated threshold values at different tube voltages of each scanner. Threshold values at 70, 80, 100, 120 and 140 kV are expressed as mean and standard deviation.

4.1.2 Inter-scanner variation in phantom density measurements

The results of the ROI measurements at different kVs for each phantom chambers are summarized in **Table 7** for Aquillion ONE, in **Table 8** for SOMATOM Force and in **Table 9** for Revolution. The inter-scanner differences are summarized in **Table 10**. The lower the tube voltage, the higher HU density was measured in the bone chambers. A different trend was observed in nearly all of the water and soft tissue chambers except for liver and solid water chambers, where the HU density was increasing with the higher tube voltage. Density values in the lung chambers did not follow any particular trend.

		80 kV	**100 kV**	**120 kV**	**135 kV**
Aquilion ONE	Lung inhale	-513.0 (36.5)	-512.2 (23.9)	-524.6 (24.5)	-520.1 (24.2)
	Lung exhale	-566.0 (27.8)	-624.7 (30.7	-659.4 (26.8)	-653.2 (26.9)
	Inner bone	296.8 (23.3)	218.9 (15.7)	192.1 (11.4)	192.7 (9.8)
	Bone 1.15	292.7 (24.1)	227.0 (14.5)	207.7 (12.1)	201.2 (9.8)
	Bone 1.34	575.4 (28.2)	469.2 (16.7)	420.8 (12.8)	398.1 (11.4)
	Bone 1.56	1031.0 (30.0)	836.2 (19.8)	758.1 (15.4)	705.3 (28.9)
	Bone 1.82	1537.2 (30.0)	1252.9 (21.5)	1139.6 (18.1)	1046.0 (13.3)
	True water	5.4 (23.1)	15.1 (13.7)	13.4 (10.8)	19.6 (9.8)
	Solid water	7.4 (21.7)	8.1 (12.6)	-1.6 (10.3)	-0.2 (9.5)
	Adipose 0.92	-111 (21.6)	-92.5 (12.6)	-82.5 (9.8)	-85.4 (8.9)
	Breast 0.99	-63.7 (22.1)	-18.2 (16.2)	-42.9 (9.7)	-48.1 (8.8)
	Brain 1.05	76.5 (26.1)	88.9 (15.5)	108.4 (12.9)	104.5 (10.7)
	Liver 1.08	83.1 (21.1)	70.0 (12.7)	52.6 (9.9)	64.3 (8.9)

Table 7: Results of ROI measurements with Aquillion ONE CT scanner. For each phantom density the first value represents the mean denstity (in HU), the second value in brackets represents the image noise (in HU).

		70 kV	80 kV	90 kV	100 kV	110 kV	120 kV	130 kV	140 kV
SOMATOM Force	Lung inhale	-520.3 (20.0)	-533.0 (22.2)	-531.0 (22.7)	-537.7 (22.5)	-540.3 (20.3)	-538.7 (21.3)	-539.7 (22.0)	-536.3 (21.8)
	Lung exhale	-653.3 (50.3)	-672.7 (27.0)	-671.0 (24.0)	-679.3 (27.3)	-681.0 (30.2)	-682.7 (27.0)	-681.7 (24.1)	-683.3 (23.4)
	Inner bone	339.0 (16.8)	295.3 (12.6)	261.7 (10.4)	245.0 (8.9)	224.3 (8.5)	210.3 (7.6)	196.7 (6.9)	190.3 (6.9)
	Bone 1.15	340.7 (15.8)	301.3 (12.6)	270.3 (10.5)	250.0 (9.1)	230.7 (8.6)	214.3 (7.3)	205.7 (7.7)	196.3 (7.1)
	Bone 1.34	638.0 (20.5)	582.0 (14.5)	527.0 (14.4)	498.3 (11.9)	471.0 (10.1)	449.0 (8.9)	423.7 (10.3)	415.3 (8.4)
	Bone 1.56	1176.3 (27.1)	1054.7 (20.6)	954.3 (16.5)	896.0 (13.8)	841.3 (12.8)	794.7 (10.8)	752.3 (11.8)	727.3 (10.6)
	Bone 1.82	1815.0 (30.2)	1595.0 (20.9)	1443.3 (19.4)	1344.0 (15.4)	1271.0 (15.6)	1196.3 (12.0)	1129.3 (11.5)	1084.3 (11.5)
	True water	-2.3 (14.7)	6.3 (11.7)	8.0 (9.9)	14.7 (10.2)	22.0 (8.1)	26.7 (7.7)	24.0 (7.6)	33.0 (7.2)
	Solid water	6.3 (12.2)	8.2 (1.9)	5.2 (9.1)	3.8 (7.8)	5.3 (7.3)	4.9 (6.6)	1.8 (1.5)	5.3 (6.6)
	Adipose 0.92	-117 (11.9)	-104.0 (9.3)	-97.7 (7.9)	-94.0 (7.8)	-86.7 (6.8)	-85.0 (6.9)	-84.0 (6.2)	-82.3 (6.3)
	Breast 0.99	-65.0 (15.1)	-57.3 (9.7)	-52.3 (8.5)	-50.3 (7.6)	-47.0 (6.3)	-40.7 (6.6)	-45.7 (6.1)	-42.0 (6.5)
	Brain 1.05	94.6 (15.1)	106.3 (12.7)	108.3 (12.1)	116.7 (10.3)	127.3 (9.4)	128.0 (8.4)	126.7 (8.2)	131.7 (8.2)
	Liver 1.08	82.0 (14.8)	76.3 (9.9)	73.0 (8.7)	75.7 (7.7)	74.0 (7.0)	75.0 (6.8)	69.7 (6.9)	76.3 (6.5)

Table 8: Results of ROI measurements with Siemens Force CT scanner. For each phantom density the first value represents the mean density (in HU), the second value in brackets represents the image noise (in HU).

		70 kV	80 kV	100 kV	120 kV	140 kV
Revolution	Lung inhale	-515.5 (29.6)	-532.2 (100.9)	-541.8 (108.2)	-540.8 (101.1)	-556.1 (138.3)
	Lung exhale	-643.1 (30.1)	.659.9 (36.3)	-672.8 (36.9)	-678.2 (33.1)	-704.6 (37.6)
	Inner bone	293.5 (20.7)	237.3 (18.1)	194.1 (11.6)	176.4 (10.0)	154.1 (8.8)
	Bone 1.15	318.9 (23.3)	279.1 (19.4)	231.2 (13.3)	104.9 (9.0)	187.2 (8.8)
	Bone 1.34	606.9 (30.4)	547.8 (22.4)	466.6 (16.3)	425.3 (12.2)	395.6 (11.0)
	Bone 1.56	1146.7 (37.7)	1023.5 (27.3)	873.4 (19.4)	785.1 (15.5)	719.3 (13,7)
	Bone 1.82	1780.8 (64.2)	1584.5 (42.0)	1343.6 (25.7)	1206.1 (21.1)	1131.4 (18.5)
	True water	-7.9 (20.9)	-8.7 (19.4)	3.8 (13.1)	6.6 (9.6)	12.8 (8.1)
	Solid water	-1 (20.5)	1.8 (17.6)	-1.6 (11.1)	-7.3 (8.7)	-6.6 (7.5)
	Adipose 0.92	-121.0 (19.1)	-112.1 (15.6)	-102.1 (12.1)	-98.3 (8.8)	-104 (7.3)
	Breast 0.99	-65.0 (21.2)	-62.1 (15.6)	-58.9 (11.1)	-58.0 (9.2)	-58.9 (4.7)
	Brain 1.05	42.3 (25.2)	74.9 (20.8)	93.2 (15.0)	97.9 (11.4)	103.3 (10.4)
	Liver 1.08	64.2 (19.2)	61.4 (16.3)	61.4 (11.2)	57.5 (8.3)	58.6 (7.4)

Table 9: Results of ROI measurements with Revolution CT scanner. For each phantom density the first value represents the mean density (in HU), the second value in brackets represents the image noise (in HU).

Table 10:

		70 kV	**80 kV**	**100 kV**	**120 kV**	**140 kV**
Lung inhale	Aquilion ONE vs Force	-	0.059	**0.002**	0.308	-
	Aquilion ONE vs Revolution	-	**0.039**	**0.001**	0.207	-
	Force vs Revolution	0.572	1.000	1.000	1.000	0.198
Lung exhale	Aquilion ONE vs Force	-	**0.0001**	**<0.0001**	0.059	-
	Aquilion ONE vs Revolution	-	**0.0001**	**<0.0001**	0.131	-
	Force vs Revolution	0.402	0.148	0.366	1.000	0.188
Bone 1.12	Aquilion ONE vs Force	-	1.000	**<0.0001**	**0.002**	-
	Aquilion ONE vs Revolution	-	**<0.0001**	**0.001**	**0.005**	-
	Force vs Revolution	**0.0157**	**<0.0001**	**<0.0001**	**<0.0001**	**0.0084**
Bone 1.15	Aquilion ONE vs Force	-	**0.029**	**<0.0001**	0.125	-
	Aquilion ONE vs Revolution	-	**0.003**	0.334	0.986	-
	Force vs Revolution	**0.0208**	**<0.0001**	**0.001**	**0.032**	**0.059**
Bone 1.34	Aquilion ONE vs Force	-	0.321	**0.032**	**0.004**	-
	Aquilion ONE vs Revolution	-	**0.001**	1.000	1.000	-
	Force vs Revolution	0.128	**<0.0001**	**0.022**	**0.011**	**0.022**
Bone 1.56	Aquilion ONE vs Force	-	**0.020**	**0.001**	**0.007**	-
	Aquilion ONE vs Revolution	-	0.732	**0.012**	**0.029**	-
	Force vs Revolution	0.245	**0.005**	0.101	0.704	0.330
Bone 1.82	Aquilion ONE vs Force	-	**0.001**	**0.001**	**0.013**	-
	Aquilion ONE vs Revolution	-	**0.003**	**0.001**	**0.006**	-
	Force vs Revolution	0.138	0.659	1.000	1.000	0.267
True water	Aquilion ONE vs Force	-	1.000	1.000	**0.006**	-
	Aquilion ONE vs Revolution	-	**0.004**	0.153	0.111	-
	Force vs Revolution	**0.0027**	**0.003**	0.175	**0.001**	0.473
Solid water	Aquilion ONE vs Force	-	1.000	0.277	**0.005**	-
	Aquilion ONE vs Revolution	-	**0.009**	**0.002**	**0.013**	-
	Force vs Revolution	**0.017**	**0.003**	0.116	**< 0.001**	**0.0003**
Adipose	Aquilion ONE vs Force	-	0.154	0.893	0.131	-
	Aquilion ONE vs Revolution	-	1.000	**0.001**	**<0.0001**	-
	Force vs Revolution	0.527	0.110	**0.002**	**<0.0001**	**0.022**
Breast 0.99	Aquilion ONE vs Force	-	0.102	**<0.0001**	0.489	-
	Aquilion ONE vs Revolution	-	1.000	**<0.0001**	**<0.0001**	-
	Force vs Revolution	0.995	0.261	**0.033**	**<0.0001**	**0.0002**
Brain 1.05	Aquilion ONE vs Force	-	**<0.0001**	**0.002**	**<0.0001**	-
	Aquilion ONE vs Revolution	-	1.000	1.000	**0.009**	-
	Force vs Revolution	**0.0036**	**<0.0001**	**0.004**	**<0.001**	**0.0172**
Liver 1.08	Aquilion ONE vs Force	-	**0.009**	0.384	**<0.0001**	-
	Aquilion ONE vs Revolution	-	**<0.0001**	0.108	0.197	-
	Force vs Revolution	**0.0204**	**<0.0001**	**0.013**	**0.001**	**0.0014**

Table 10: Summary of the inter-scanner differences at the common tube voltages and for each phantom chambers. Significant differences are marked bold.

Figure 18 demonstrates the differences between the measured HU on each respective scanner and the mean phantom density measured on all three scanners. Generally, less deviations were observed in case of the physical densities close to that of water (soft tissue and water chambers). In the meantime, larger discrepancies were detected in case of physical densities far from the water density (lung and bone chambers). Except for the breast and lung chambers, SOMATOM Force measured constantly higher HU values compared to the mean HU values. On the contrary, the Revolution scanner measured constantly lower HU densities than the mean density, except for two tissue-mimicking bone chambers with the higher physical densities. Measurements with Aquilion ONE deviated in both directions without any clear trend. The higher the physical density in the bone chambers, the larger decrease was observed in the HU values measured by Aquilion ONE in comparison to the mean HU.

An interesting relationship was observed between the true water HU values and the tube voltage settings. All of the CT scanners measured increasing HU values at higher tube voltages with the largest range of -2.3 and 33.0 HU in case of SOMATOM Force.

Figure 18:

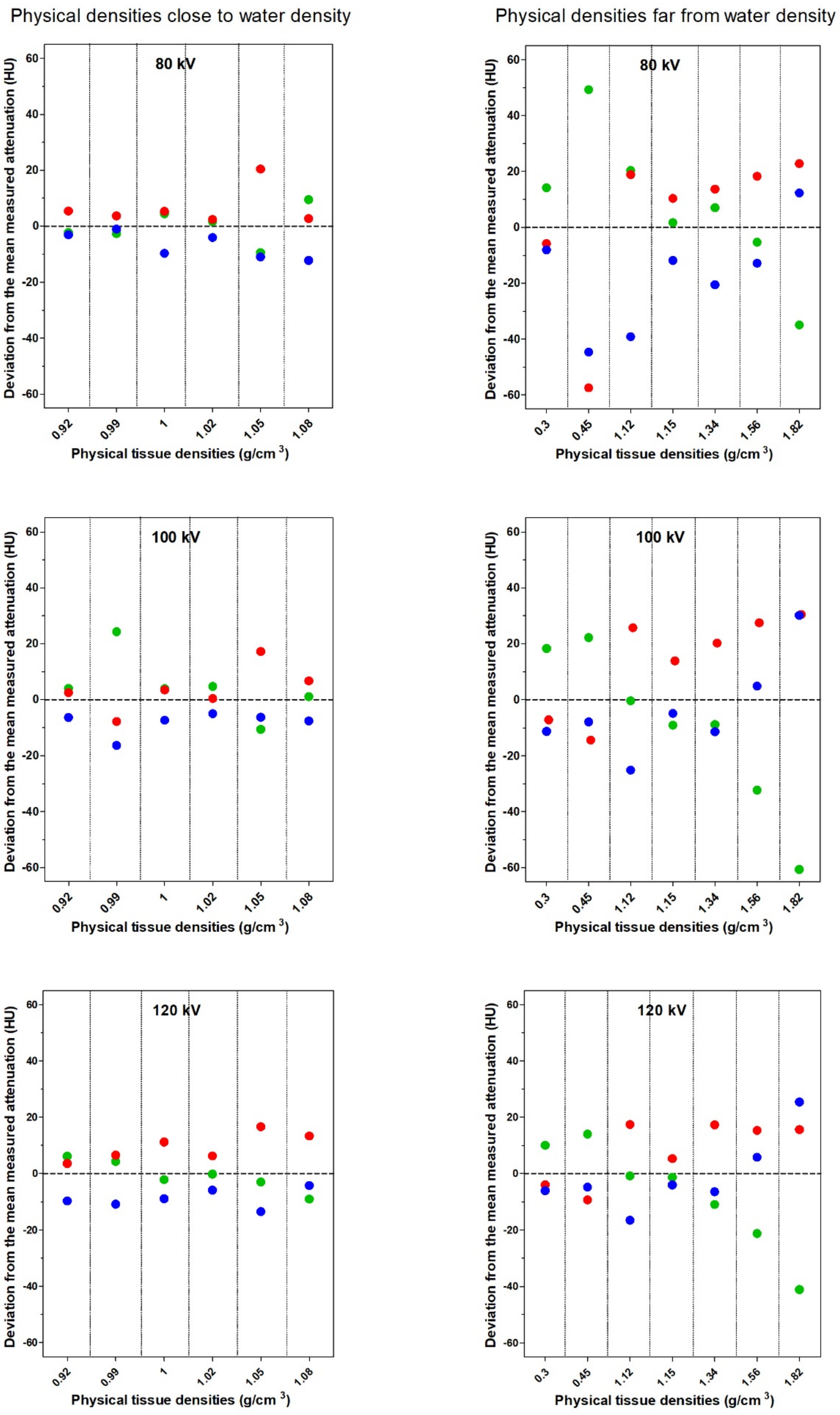
Physical densities close to water density
Physical densities far from water density
80 kV
100 kV
120 kV
Deviation from the mean measured attenuation (HU)
60
40
20
0
-20
-40
-60
0.92
0.99
1
1.02
1.05
1.08
0.3
0.45
1.12
1.15
1.34
1.56
1.82
Physical tissue densities (g/cm 3)

Figure 18: Interscanner variations in HU at 80 kV (top), at 100 kV (middle) and at 120 kV (bottom). The line at y = 0 corresponds to the mean HU of all CT scanners (n=3). Measurements on Aquilion ONE signed with green, on SOMATOM Force with red, and on Revolution with blue circles.

Despite the differences in the measured HU values, Bland-Altman analysis has ruled out any systematic bias between two respective scanners, as indicated in **Figure 19 and 20**. However, the supplementary linear regression revealed significant differences in the comparison of the "newer scanners" (SOMATOM Force and Revolution) and the "older" scanner (Aquilion ONE).

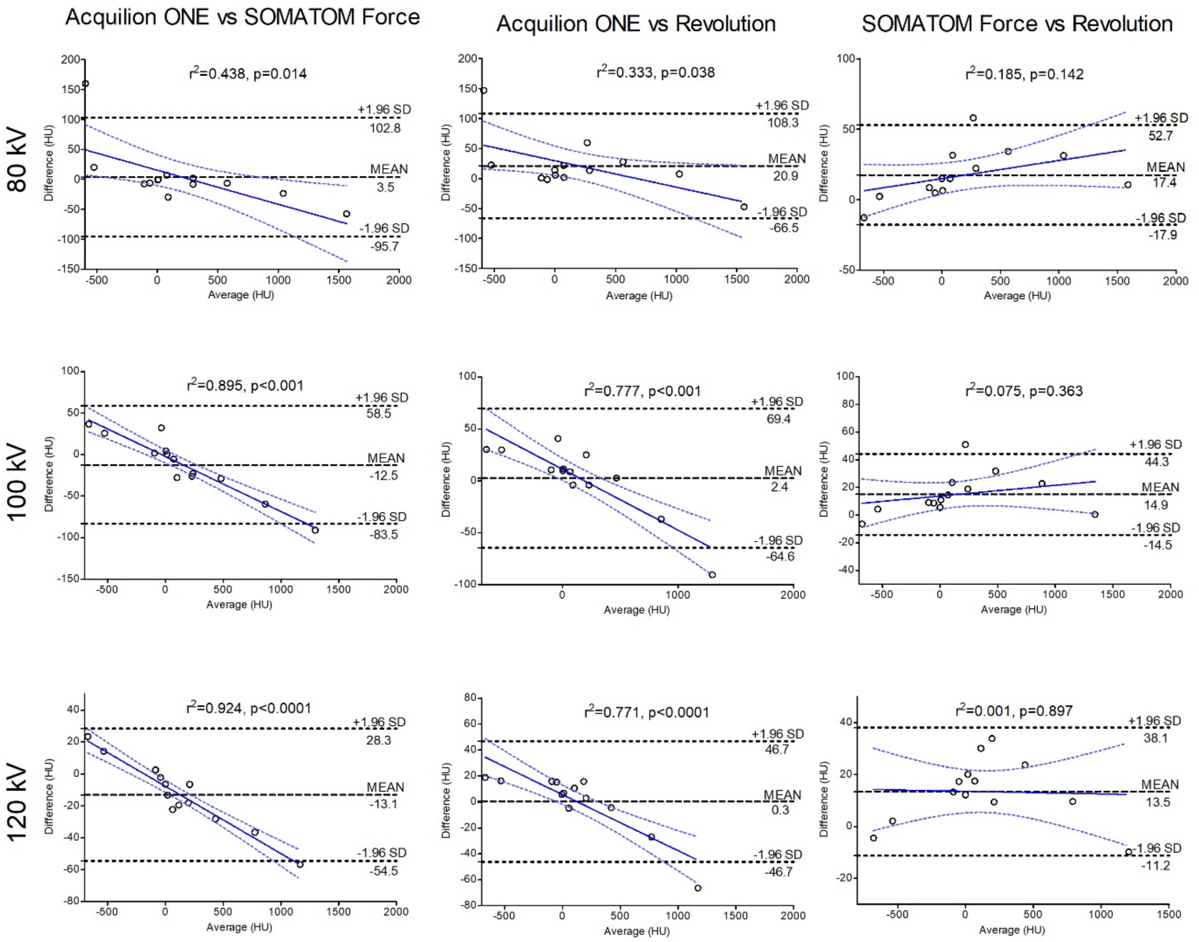

Figure 19: Bland-Altman comparison of the measured attenuations at 80, 100, and 120 kV on three different scanners. A linear regression analysis was added, as well.

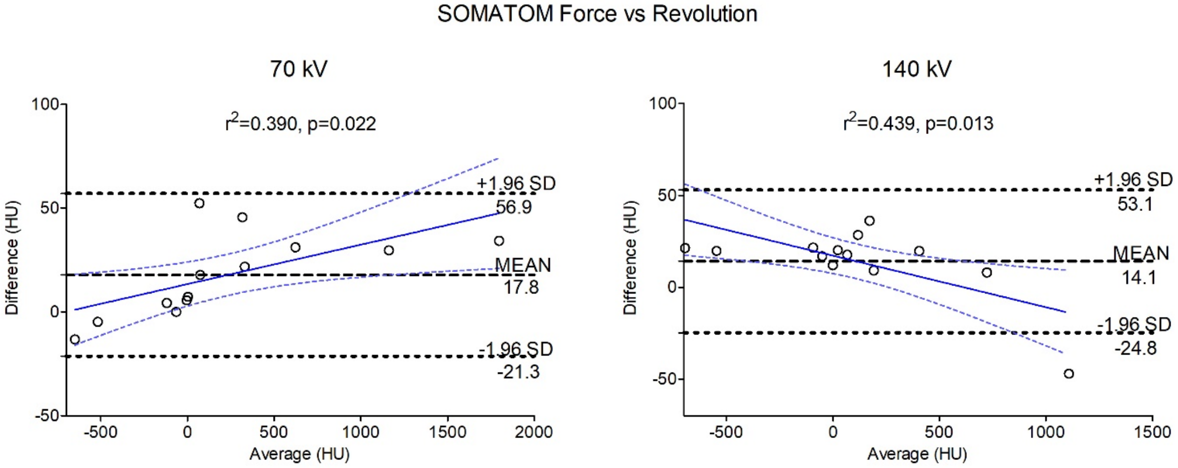

Figure 20: Bland-Altman comparison of SOMATOM Force and Revolution scanners with added linear regression at 70 and 140 kV.

4.2 Patients

The current chapter is based on the original article of Nagy et al. "Chest CTA in children younger than two years - a retrospective comparison of three contrast injection protocols", published in Scientific Reports 2019 (61).

4.2.1 Baseline patient characteristics

Table 11 summarizes the baseline patient characteristics. There was no significant difference regarding patient age, weight, and effective diameter (p > 0.05), although patients in group II and III were slightly older and had a little more bodyweight. Heterogeneous distribution of primary diseases was found. Most of the patients suffered in a lung disorder (n=26) followed by vascular disorders (n=21). Among the congenital lung disorders, 12 patients were diagnosed with congenital pulmonary airway malformation (CPAM), while two patients suffered in pulmonary hypoplasia and congenital lobar overinflation, as well. Among the vascular diseases, most of the patients had pulmonary vein abnormalities (n=9), which was followed by sequesters (n=5). Variable primary cardiac disorders occurred in the examined patient cohort, like tetralogy of Fallot, univentricular heart, atrioventricular canal defect, truncus arteriosus, hypoplastic left heart syndrome, and Ebstein anomaly. Patients with Fontan circulation did not occur in the study population. Tracheal stenosis and tracheomalacia were classified as tracheobronchial disorders, while esophageal atresia and a pericardial cyst belonged to mediastinal disorders. The miscellaneous group contained patients with diaphragmatic hernia or examinations without any apparent pathologies.

	Group I (n=32)	**Group II** (n=23)	**Group III** (n=15)	**p**
Patient age (months, mean ± SD)	5.8 ± 5.2	7.7 ± 6.4	7.4 ± 5.1	0.411
Patient weight (kg, mean ± SD)	5.7 ± 2.5	6.8 ± 2.6	7.0 ± 2.0	0.149
Effective diameter (mm, mean ± SD)	126.4 ± 14.0	119.8 ± 16.5	129.1 ± 14.0	0.108
Underlying diseases (n, %)				
Extracardiac vascular (n=22)	10 (31.2%)	11 (47.8%)	1 (6.7%)	-
Vascular rings (n)	1	1	-	-
Pulmonary vein abnorm. (n)	3	6	-	-
Coarctation of aorta (n)	2	1	1	-
Sequester (n)	3	2	-	-
Miscellaneous (n)	1	1	-	-
Cardiac (n=9)	5 (15.5%)	4 (17.4%)	-	-
Tetralogy of Fallot (n)	2	1	-	-
Univentricular heart (n)	1	-	-	-
Miscellaneous (n)	2	3	-	-
Tracheobronchial (n=6)	2 (6.3%)	3 (13%)	1 (6.7%)	-
Mediastinal (n=2)	2 (6.3%)	-	-	-
Lung (n=26)	11 (34.4%)	4 (17.4%)	11 (73.3%)	-
Congenital (n)	8	4	2	-
Infection (n)	3	-	3	-
Malignancy (n)	0	-	6	-
Miscellaneous (n=5)	2 (6.3%)	1 (4.0%)	2 (13.3%)	-

Table 11: Baseline patient characteristics (61).

4.2.2 Technical data

Table 12 summarizes all exposure and image reconstruction data. All examinations were performed at 80 kV. The tube current was significantly lower in group I than in group II and group III (p=0.002 group I vs II; p=0.046 group I vs III, respectively). Images were acquired in volume mode in the majority of the cases (87% in group I, 91% in group II and 60% in group III, respectively).

In 75% of the examinations in group I an iterative reconstruction with AIDR was performed. The proportion of AIDR was substantially less in the other two groups (26% in group II and 20% in group III).

The values of the radiation dose were compared with each other based on the presence or absence of iterative reconstruction. In the cases with activated AIDR, no significant differences were found between the groups concerning DLP (p= 1.000 group I vs II; p=0.530 group I vs III; p=0.621 group II vs III), CTDIvol (p=0.997 group I vs II; p=0.274 group I vs III; p=0.400 group II vs group III) and SSDE (p=0.341 group I vs II; p=0.564 group I vs III; p=0.183 group II vs group III). Similarly, no significant differences were found between the groups concerning DLP (p=0.638 group I vs II; p=0.991 group I vs III; p=0.470 group II vs III), CTDIvol (p=0.643 group I vs II; p=0.820 group I vs III; p=0.953 group II vs III) and SSDE (p=0.661 group I vs II; p=0.313 group I vs III; p=0.706 group II vs III) in the cases with inactivated AIDR.

Images were reconstructed with FC17 kernel in 65.2% of the cases in group II and in 66.6% of the cases in group III. 81.2% of the examination in group I was reconstructed with FC18 kernel. The applied slice thickness for image reconstruction was 3 mm in most cases (91% in group I, 70% in group II, 60% in group III, respectively).

		Group I (n=32)	**Group II** (n=23)	**Group III** (n=15)	**p** **I - II**	**p** **I - III**	**p** **II - III**
Radiation exposure	**Tube current** (mAs,median,95%CI)	50.0 (52.1, 74.0)	105 (81.5, 32.3)	90.0 (69.7, 113.2)	0.002	0.046	1.000
	Exposure time (ms, median, 95%CI)	500.0	500.0 (486.0, 504.9)	500 (461.7, 662.7)	1.000	0.021	0.006
	Eff. tube current (mAs, median,95%CI)	25.0 (26.9, 40.2)	58.0 (44.1, 67.9)	45.0 (-171.2, 636.1)	0.001	0.036	1.000
	Scan length (cm, median, 95%CI)	13.8 (-12.2, 88.3)	13.7 (11.9, 14.5)	12.2 (11.3, 15.1)	-		
	Volume CT (n)	28 (87%)	21 (91%)	9 (60%)	-		
	DLP (mGy.cm, mean±SD)	41.2 ± 26.1	54.1 ± 34.1	40.9 ± 29.8	-		
	AIDR +	35.3 (27.2, 50.7)	38.8 ± 34.9	5.7 (-40.4, 79.8)	1.000	0.530	0.621
	AIDR -	47.9 ± 20.2	59.5 ± 33.1	46.3 ± 29.5	0.638	0.991	0.470
	CTDI$_{vol}$ (mGy, mean ± SD)	2.1 ± 1.1	3.2 ± 1.6	2.9 ± 1.9	-		
	AIDR +	1.8 ± 0.9	1.8 ± 1.4	0.6 (-0.7, 2.5)	0.997	0.274	0.400
	AIDR -	3.1 ± 1.3	3.6 ± 1.5	3.5 ± 1.8	0.643	0.820	0.953
	SSDE (mGy, mean ± SD)	2.7 ± 1.2	4.1 ± 1.9	4.2 ± 2.7	-		
	AIDR +	2.4 ± 0.8	2.6 (0.2, 6.3)	1.4 (0.6, 2.8)	0.341	0.564	0.183
	AIDR -	3.6 ± 1.6	4.3 ± 1.6	4.9 ± 2.5	0.661	0.313	0.706
Image reconstruction	**AIDR active** (n)	24 (75%)	6 (26%)	3 (20%)	-		
	Soft tissue kernel (n)						
	FC17	6 (18.8%)	15 (65.2%)	10 (66.6%)	-		
	FC18	26 (81.2%)	6 (26.1%)	3 (20%)	-		
	FC14	0	2 (8.7%)	1 (6.7%)	-		
	other	0	0	1 (6.7%)	-		
	Slice thickness in soft tissue reconstruction, axial (n)						
	3 mm	29 (91%)	16 (70%)	9 (60%)	-		
	2 mm	3 (9%)	5 (22%)	2 (13.3%)	-		
	other	0	2 (8%)	4 (26.7%)	-		

Table 12: Data on radiation exposure and image reconstruction [adapted and modified after (61)].

4.2.3 Contrast agent application in thoracic CTs

According to the study inclusion criteria, patients received a CA with 300 mg iodine/ml concentration. 62.8% of the patients obtained Iomeprol (Iomeron300); otherwise, Iopamidol (Jopamiro300) with slightly higher osmolarity was injected for the CTAs. Significantly less amount of CA (absolute and bodyweight-adjusted) was applied in group I compared to group II (9.0 ± 3.7 ml vs. 12.9 ± 4.5 ml; p=0.005 and 1.8 ± 0.7 ml/kg and 2.0 ± 0.5 ml/kg respectively, p=0.012) (**Table 12**).No significant differences were found in the applied amount of CA between group I and group III, as well as group II and group III, as indicated in **Table 13**.

	Group I n=32 (mean ± SD)	**Group II** n=23 (mean ± SD)	**Group III** n=15 (mean ± SD)	**p I - II**	**p I - III**	**p II - III**
CA (ml)	9.0 ± 3.7	12.9 ± 4.5	12.1 ± 5.2	**0.005**	0.151	0.316
CA (ml/kg)	1.8 ± 0.7	2.0 ± 0.5	1.7 ± 0.5	**0.012**	0.757	0.068
Iomeprol (Iomeron300) 521 ± 24 osm/kg (n)	32 (100%)	8 (34.8%)	4 (26.7%)	-	-	-
Iopamidol (Jopamiro300) 616 osm/kg (n)	0	15 (65.2%)	11 (73.3%)	-	-	-

Table 13: Applied CA in each group for contrast-enhanced thoracic CT (61). Significant differences are marked bold.

4.2.4 Objective assessment of image quality

Figure 21 demonstrates an illustrative comparison of the three CA application protocols with ROI measurements. Significantly lower but diagnostic (more than 400 HU) enhancement was measured in the following regions of group I compared to group II, as indicated in **Figure 22** and **Table 14**: in all three regions of the thoracic aorta (p=0.001 for AA, p=0.004 for AAr, and p=0.001 for AD), in the superior cava vein (p=0.033), in the left-sided heart chambers (p=0.001 for LA and p=0.001 for LV), and the right ventricle (p=0.041). Mean enhancement in all three regions of the aorta (p=0.005 for AA, p=0.014 Aar, and p=0.017 for AD) and in the left-sided heart chambers (p=0.005 for LA and p=0.009 for LV) was significantly lower in group I than in group III. Significantly less image noise was recorded in the ascending aorta (p=0.010), in the left-sided heart chambers (p=0.002 for LA and 0.038 for LV), and right-upper pulmonary vein (p=0.036) of group I compared to group II. The image noise comparison between group I and III revealed comparable results in most of the regions. However, image noise was significantly lower in the left atrium of group I than of group III (p=0.005). There was no significant difference in the image noise between group II and group III.

The comparison of SNR values showed just a few significant differences, as follows (**Figure 23**): in the descending aorta between group I and II (p=0.005), in the aortic arch and right ventricle between group I and III (p=0.042 and p=0.013. respectively), as well as in the right ventricle between group II and III (p=0.036). Except for the measurement in the descending aorta (p=0.041 between group I and II), there was no difference between the groups regarding the CNR values (**Figure 23**).

The comparison of the contrast enhancement between the different vascular regions in one group revealed no significant differences (in group I p=0.076, in group II p=0.106, in group III p=0.091), which indicates a homogenous enhancement in all thoracic CT, regardless the applied CA protocol.

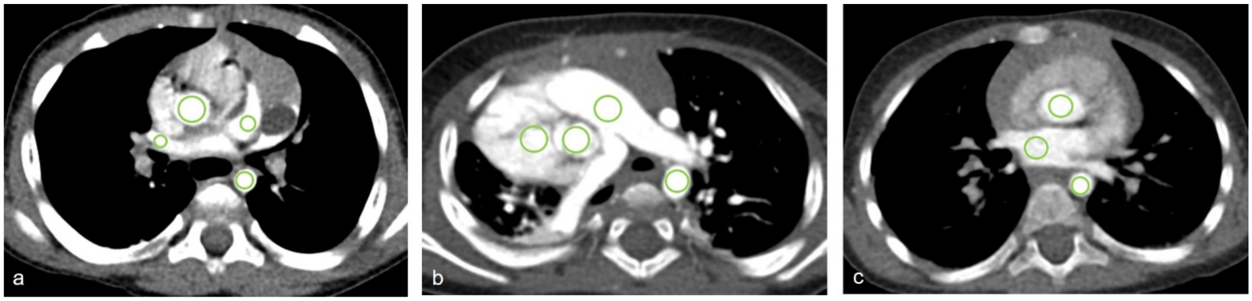

Figure 21: Comparison of three contrast agent application protocols using representative CT images. a: 4-month- old male patient with a suspected mediastinal mass. CT angiography was performed with microbolus technique. The acquired mean enhancement values from right to left are as follows: 356 HU in the right upper pulmonary vein, 480 HU in the ascending aorta, 435 HU in the left atrium, and 498 HU in the descending aorta. **b**: 12-month-old male patient with Scimitar syndrome and suspected pulmonary sequester. The contrast agent was injected according to the protocol of group II. The acquired mean enhancement values from right to left are as follows: 576 HU in the right ventricle, 723 HU in the ascending aorta, 653 HU in the pulmonary trunk, and 692 HU in the descending aorta. **c**: 16-month-old male patient with rhabdomyosarcoma subjected to staging CT. The contrast agent was injected according to the protocol of group III with 8 sec delay. The acquired mean enhancement values from right to left are as follows: 387 HU in the left atrium, 413 HU in the ascending aorta, and 415 HU in the descending aorta. Abbreviation: HU for Hounsfield unit

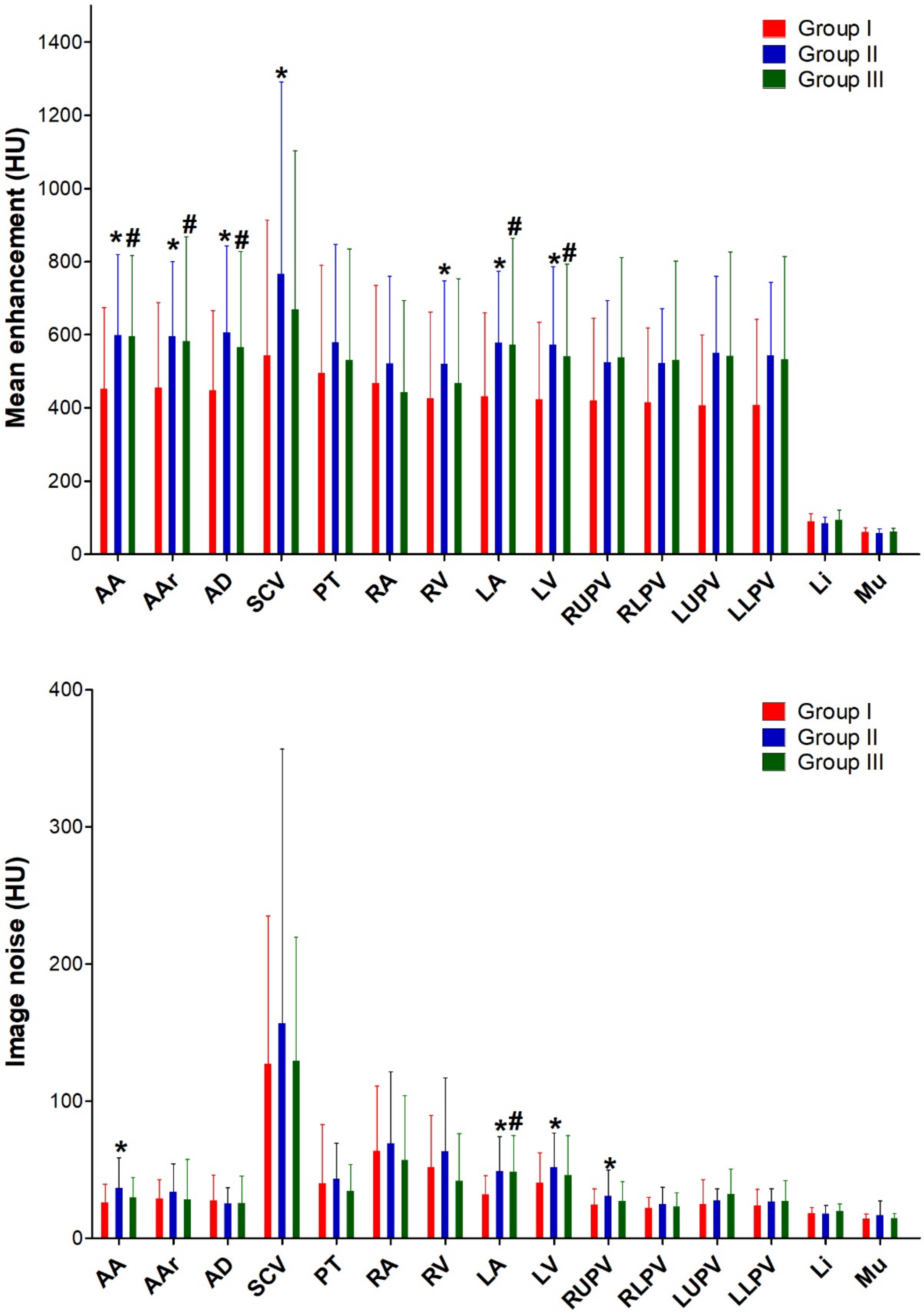

Figure 22: Mean enhancement (upper image) and image noise (bottom image) [adapted and modified after (61)]. *: significant difference between group I and II, #: significant difference between group I and III, §: significant difference between group II and III

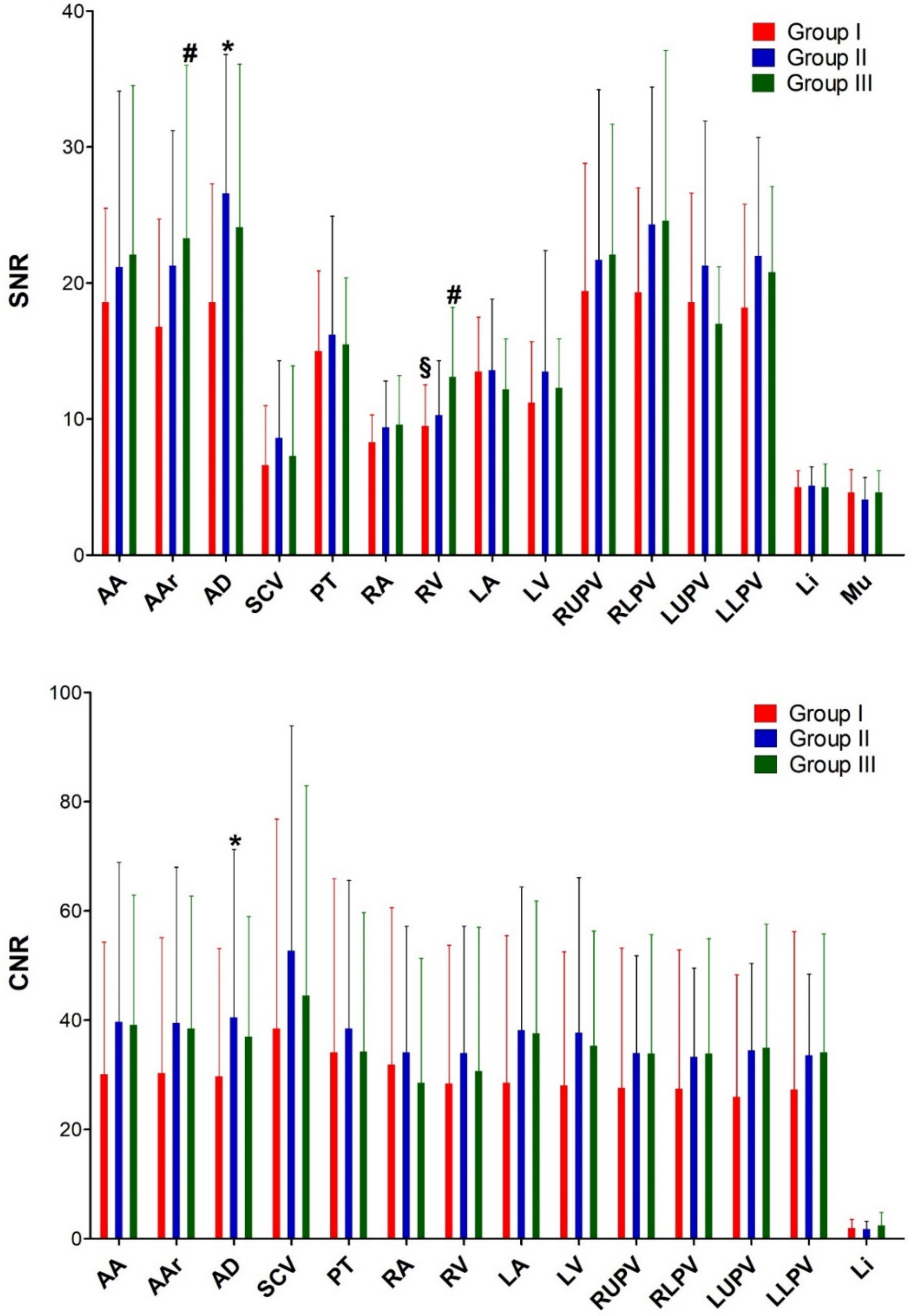

Figure 23: Bar chart depiction of the SNR (upper image) and CNR (bottom image) measurements [adapted and modified after (61)]. *: significant difference between group I and II, #: significant difference between group I and III, §: significant difference between group II and III

Table 14:

	Variable	**Group I** n=32 (mean ± SD)	**Group II** n=23 (mean ± SD)	**Group III** n=15 (mean ± SD)	**p** **I - II**	**p** **I - III**	**p** **II - III**
Ascending aorta	*Enhancement*	452.8 ± 221.2	599.7 ± 220.3	596.2 ± 221.3	**0.001**	**0.005**	0.927
	Image noise	25.8 ± 13.7	36.7 ± 22.1	29.7 ± 14.4	**0.010**	0.322	0.215
	SNR	18.6 ± 6.9	21.2 ± 12.9	22.1 ± 12.4	0.347	0.263	0.768
	CNR	30.1 ± 24.2	39.7 ± 29.2	39.1 ± 23.8	0.055	0.088	0.969
Aortic arch	*Enhancement*	455.1 ± 233.4	596.7 ± 202.4	581.8 ± 287.1	**0.004**	**0.014**	0.942
	Image noise	28.8 ± 13.9	33.9 ± 20.5	28.2 ± 29.4	0.076	0.597	0.323
	SNR	16.8 ± 7.9	21.3 ± 9.9	23.3 ± 12.7	0.118	**0.042**	0.501
	CNR	30.3 ± 24.8	39.5 ± 28.5	38.5 ± 24.2	0.073	0.121	0.988
Descending aorta	*Enhancement*	448.0 ± 218.5	606.8 ± 236.4	565.1 ± 262.7	**0.001**	**0.017**	0.639
	Image noise	27.4 ± 18.6	25.2 ± 11.7	25.6 ± 19.7	0.959	0.892	0.930
	SNR	18.6 ± 8.7	26.6 ± 10.2	24.1 ± 12.0	**0.005**	0.071	0.520
	CNR	29.7 ± 23.4	40.5 ± 30.7	37.0 ± 22.0	**0.041**	0.149	0.737
Superior cava vein	*Enhancement*	543.5 ± 369.5	766.1 ± 525.7	669.6 ± 433.6	**0.033**	0.211	0.545
	Image noise	126.9 ± 108.1	156.6 ± 200.0	129.2 ± 90.3	0.386	0.861	0.575
	SNR	6.6 ± 4.4	8.6 ± 5.7	7.3 ± 6.6	0.229	0.784	0.453
	CNR	38.5 ± 38.3	52.7 ± 41.2	44.5 ± 38.4	0.084	0.339	0.588
Pulmonary trunk	*Enhancement*	495.7 ± 294.9	580.6 ± 267.1	531.5 ± 303.2	0.070	0.248	0.674
	Image noise	39.9 ± 43.0	43.2 ± 26.2	34.6 ± 19.4	0.477	0.942	0.504
	SNR	15.0 ± 5.9	16.2 ± 8.7	15.5 ± 4.9	0.419	0.701	0.757
	CNR	34.1 ± 31.8	38.5 ± 27.1	34.3 ± 25.4	0.219	0.469	0.734
Right atrium	*Enhancement*	467.1 ± 267.6	521.7 ± 238.6	442.5 ± 251.2	0.145	0.713	0.380
	Image noise	63.7 ± 47.3	68.3 ± 51.9	56.9 ± 47.3	0.458	0.984	0.519
	SNR	8.3 ± 2.0	9.4 ± 3.4	9.6 ± 3.6	0.213	0.196	0.837
	CNR	31.9 ± 28.7	34.1 ± 23.1	28.6 ± 22.7	0.337	0.798	0.572
Right ventricle	*Enhancement*	426.7 ± 235.7	520.3 ± 227.1	467.9 ± 285.1	**0.041**	0.225	0.578
	Image noise	51.9 ± 37.7	63.3 ± 53.5	42.0 ± 34.2	0.131	0.864	0.155
	SNR	9.5 ± 3.0	10.3 ± 4.0	13.1 ± 5.1	0.699	**0.013**	**0.036**
	CNR	28.4 ± 25.3	34.0 ± 23.2	30.7 ± 26.3	0.159	0.353	0.772
Left atrium	*Enhancement*	431.2 ± 229.5	578.4 ± 195.9	573.2 ± 290.8	**0.001**	**0.005**	0.939
	Image noise	31.9 ± 13.8	48.8 ± 25.2	48.4 ± 26.5	**0.002**	**0.005**	0.971
	SNR	13.5 ± 4.0	13.6 ± 5.2	12.2 ± 3.7	0.698	0.494	0.328
	CNR	28.6 ± 26.9	38.2 ± 26.2	37.6 ± 24.2	0.056	0.089	0.972
Left ventricle	*Enhancement*	423.6 ± 211.3	572.8 ± 213.4	541.2 ± 251.7	**0.001**	**0.009**	0.748
	Image noise	40.3 ± 22.0	51.9 ± 24.8	45.9 ± 28.8	**0.038**	0.286	0.467
	SNR	11.2 ± 4.5	13.5 ± 8.9	12.3 ± 3.6	0.099	0.309	0.682

	CNR	28.1 ± 24.4	37.7 ± 28.4	35.3 ± 21.0	0.052	0.132	0.850
Right upper pulmonary vein	*Enhancement*	420.4 ± 224.5	523.8 ± 169.6	537.4 ± 273.9	0.051	0.486	0.663
	Image noise	24.4± 11.6	30.7 ± 19.0	27.2 ± 14.3	**0.036**	0.204	0.627
	SNR	19.4 ± 9.4	21.7 ± 12.5	22.1 ± 9.6	0.493	0.431	0.835
	CNR	27.6 ± 25.6	34.0 ± 17.8	33.9 ± 21.8	0.171	0.178	0.846
Right lower pulmonary vein	*Enhancement*	414.9 ± 205.0	522.7 ± 149.0	530.4 ± 271.3	0.092	0.606	0.884
	Image noise	22.0 ± 7.6	25.0 ± 12.0	22.8 ± 10.1	0.101	0.344	0.654
	SNR	19.3 ± 7.7	24.3 ± 10.1	24.6 ± 12.5	0.052	0.101	0.981
	CNR	27.5 ± 25.4	33.3 ± 16.2	33.9 ± 21.0	0.148	0.178	0.912
Left upper pulmonary vein	*Enhancement*	406.0 ± 193.0	549.8 ± 210.0	542.1 ± 285.3	0.110	0.766	0.983
	Image noise	25.0 ± 18.0	27.5 ± 8.4	32.4 ± 18.4	0.341	0.091	0.385
	SNR	18.6 ± 8.0	21.3 ± 10.6	17.0 ± 4.2	0.214	0.728	0.172
	CNR	26.0 ± 22.3	34.5 ± 15.9	34.9 ± 22.7	0.063	0.083	0.886
Left lower pulmonary vein	*Enhancement*	408.4 ± 234.0	543.2 ± 200.2	532.5 ± 280.5	0.106	0.719	0.994
	Image noise	23.7 ± 11.9	26.6 ± 9.6	26.9 ± 15.3	0.148	0.123	0.784
	SNR	18.2 ± 7.6	22.0 ± 8.7	20.8 ± 6.3	0.092	0.308	0.655
	CNR	27.3 ± 28.9	33.6 ± 14.8	34.1 ± 21.7	0.207	0.199	0.859
Liver	*Enhancement*	89.2 ± 21.7	84.2 ± 16.7	93.7 ± 27.3	0.688	0.283	0.175
	Image noise	18.3 ± 4.2	17.7 ± 6.2	19.7 ± 5.2	0.906	0.294	0.272
	SNR	5.0 ± 1.2	5.1 ± 1.4	5.0 ± 1.7	0.675	0.931	0.787
	CNR	2.0 ± 1.5	1.8 ± 1.4	2.4 ± 2.4	0.867	0.356	0.308
Muscle	*Enhancement*	61.3 ± 10.4	58.5 ± 11.1	62.1 ± 9.1	0.560	0.548	0.289
	Image noise	14.2 ± 3.4	16.7 ± 10.5	14.4 ± 3.4	0.115	0.721	0.327
	SNR	4.6 ± 1.7	4.1 ± 1.6	4.6 ± 1.6	0.424	0.791	0.358
	CNR	-	-	-	-	-	

Table 14: Results of the ROI measurements with the calculated SNR and CNR values (61). The significant differences are marked bold.

4.2.5 Subjective assessment of image quality

On the five-grade scale for general image quality, significantly (p=0.020) higher amount of the examinations was evaluated as "excellent or good" in group I (81.3%) compared to group II (52.2%) or group III (46.7%). A similar result was found in the assessment of the contrast-related artifacts, where 78.7% of the examinations were scored as "no or minor artifacts" in group I (p=0.006). This ratio was 52.2% in group II and 46.7% in group II. Interestingly much fewer examinations were scored with "excessive image artifacts" on the four-grade scale in group I (3%) than in group II (26%) or group III (20%). The results of the subjective image assessment are summarized in **Table15**.

General image quality (n)	**Group I (n=32)**	**Group II (n=23)**	**Group III (n=15)**
Score 1 (excellent)	16 (50%)	4 (17%)	3 (20%)
Score 2 (good)	10 (31%)	8 (35%)	4 (27%)
Score 3 (acceptable)	5 (15%)	7 (30%)	3 (20%)
Score 4 (poor)	1 (3%)	2 (9%)	5 (33%)
Score 5 (bad)	-	2 (9%)	-
CA-related image artifacts (n)			
Score 1 (no artifacts)	15 (47%)	2 (9%)	1 (7%)
Score 2 (minor artifacts)	10 (31%)	10 (43%)	6 (40%)
Score 3 (significant artifacts)	6 (19%)	5 (22%)	5 (33%)
Score 4 (excessive artifacts)	1 (3%)	6 (26%)	3 (20%)

Table 15: Results of subjective image quality assessment [adapted and modified after (61)].

5. Discussion

The current dissertation was dedicated to examine unique aspects of pediatric thoracic CT angiography. A particular focus was laid on the optimization of examination protocols in the course of a phantom study and a retrospective evaluation of three different CA application protocols.

5.1 Optimizing ABT threshold calculation based on phantom examinations with tissue-mimicking materials

An optimal ABT is essential to achieve homogenous vascular contrast enhancement in CTA and, thus, optimal image quality. On the one hand, ABT threshold values for CTA depend on the tube voltage and from the technical set up of a particular CT scanner on the other hand. The latter determines the transit delay and acquisition time. With the renaissance of the "double low concept" (98), low dose CT examinations with 70 to 100 kV are commonly performed, even in adults. As introduced in chapter 1.3.1, this approach results in less radiation dose and increased inherent iodine contrast. To avoid the inappropriate contrast timing for CTA, the tube voltage of the monitoring imaging and the following diagnostic scan should be equal. Therefore, the threshold values for the CA timing need to be adapted to altered tube voltages, as well.

In this methodological study, a reproducible way for threshold calculation using linear regression was introduced. To our best knowledge, no similar approach was proposed in the literature. Based on phantom examination with tissue-mimicking materials, several threshold values were provided for daily use. As **Figure 17** and **Table 6** indicate, switching the tube voltage from 120 to 70 kV might result in a 40% difference in the threshold value, which is required to provide the same image quality. The calculations showed just minimal inter-scanner differences, which were considered as negligible.

Since the similar methodological reports on ABT threshold calculations in the literature are scarce, the baseline assumption of this phantom study was that the reported threshold values were defined empirically at 120 kV. Therefore, in our phantom study we determined several reference thresholds at 120 kV for the purpose of threshold calculation. Three CT scanners were included in this study to gain the most comprehensive spectrum of the available tube voltage values.

Several pediatric CT studies have reported threshold values previously, but just a few of them provided complementary information on the achieved enhancement, transit delay, and the applied CA iodine concentration. In our other study with a retrospective comparison of three different CA application protocols (61), 400 HU ABT threshold was applied at 80 kV to achieve a mean aortic enhancement around 600 HU on a 320-slice volume CT scanner without transit delay. The iodine concentration of the applied CA was 300 mg iodine/ml. Based on the previously described calculations with the current phantom study, the 400 HU threshold trigger is substantially beyond the suggested ABT at 80 kV, even if the estimation was based on the highest reference threshold value. Notably, the excessive ABT threshold might lead to an avoidable increase in radiation dose during the monitoring imaging for bolus tracking.

In comparison to our study, Zapala et al. reported an enhancement of 338 ± 142 HU in the main pulmonary artery of 148 children (mean age of 11.1 years, range of 8 days to 17.9 years) with suspected pulmonary embolism (99). Schooler et al. described similar enhancement in the descendent aorta of young children (ranging from one week to five years with a mean age of 8 months) with cardiothoracic CTA (50). In both studies, the examinations were performed on a 64-slice MDCT with low tube voltage according to patient weight. The CA iodine concentration was 370 mg iodine/ml and the scans were started automatically, if the 150 HU ABT threshold was reached.

Yang et al. applied a dual-phase protocol with 350 mg iodine/ml CA at 80 kV, and the CT scan started at 80 HU ABT threshold and nine seconds threshold delay (55). With this protocol, Yang et al. received a main aortal enhancement of 460-480 HU in 61 infants (age ranging from 4 to 36 months) on cardiothoracic CTA with a 64-slice CT scanner.

Despite the higher iodine concentration of the applied CA, the previously mentioned studies reported less arterial enhancement compared to our study (61). This might be explained by the lower ABT threshold, which led to earlier contrast enhancement. Notably, the minimal required enhancement in the cardiothoracic CTA is reported variably, such as 150 HU by Yao et al. (100) or 250 HU by Thust et al. (101).

5.2 Comparison of the three CT scanners regarding measured densities

The density values on a particular CT scanner depend on the tube voltage, filtration and reconstruction algorithms. Therefore, it is reasonable to assume that the density measurements are variable between the CT scanners, and the tissue characterization based on an absolute CT might be some source of error (89).

The observed inter-scanner differences in phantom density measurements are similar to other previous studies (89, 102). In line with the result of Sande et al., more deviations were observed in the case of materials (air and bone chambers) with HU values highly different from that of the water (89). However, its relevance in the clinical routine might be negligible, since the absolute HU is not applied in the case of air and bone for tissue characterization in the daily routine. On the other hand, with regard to osteoporosis, pulmonary emphysema or chronic obstructive pulmonary disease (COPD) these differences might have a particular relevance (103-108).

Less inter-scanner variations were observed in case of soft tissue-mimicking chambers with HU values close to that of the water. In case of the brain tissue-mimicking chamber, an increasing HU value was measured with increasing tube voltages. This anomaly might be explained by the applied standard reconstruction kernel by our phantom study, which is considered inappropriate for brain imaging.

Similar to the brain chamber, an increasing HU value was observed in the true water chamber with all three CT scanners, especially in SOMATOM Force, which measured the widest range of attenuations. Beland et al. reported variable CT numbers for water, as well (109). In this study, water bottles were placed on the anterior abdominal wall of 97 patients for ROI measurements, who underwent different abdominal CT examinations. They described decreasing HU values with larger patient size, which appeared more substantial in peripheral ROI measurements. The authors concluded that density measurements in “larger patients” might result in a false interpretation of the density findings. Moreover, due to the altered density values, a possible inaccurate angiography timing was hypothesized, as well. The beam hardening effect might explain these observations, which is considered to be more pronounced at higher tube voltages. Divergent water attenuations were reported in a phantom examination by Birnbaum et al., who described a range of attenuation values between -15 HU and 20 HU for a phantom insert of 0 HU (102).

The trend of the attenuation measurement on a particular scanner is variable. Lamba et al. compared unenhanced abdominal CT examinations on Definition AS Plus (Siemens Healthcare) and Volume CT (GE Healthcare) scanners and found significantly higher attenuations on the Volume CT than on the Definition AS Plus (110). Patel et al. compared two volume scanners for whole-heart imaging and reported a general higher mean enhancement on Aquilion ONE (Toshiba/Canon) with larger variability of the HU values throughout the scan range than that of the Revolution scanner (GE Healthcare) (111). In another phantom study by Cropp et al., significantly higher air and soft tissue attenuations were reported on GE scanners than on

Siemens scanners (112). In comparison to that, the SOMATOM Force scanner measured higher attenuation values than the mean attenuation in almost all of the soft tissue and bone chambers in our sample. The clarification of the inter-scanner differences was beyond the scope of the current research project. However, the vendor-specific detector differences and reconstruction algorithms might explain the findings.

Besides the previously mentioned osteoporosis and pulmonary pathologies (emphysema/COPD), the accurate density measurements, as well as their inter-scanner variations, are relevant in several clinical applications, where the exact CT number (in HU) defines the diagnosis. The evaluation of the cystic intrarenal lesions is a typical example of this issue. According to the updated Bosniak classification, a lesion is considered as a benign cyst if the density ranges from -9 to 20 HU or over 70 HU at a native scan, as well as the density is less than 30-40 HU on the portal-venous phase CT scan (113). Enhancing lesion is defined by 20 HU increase in density. The artificial increase in the enhancement pattern (also called pseudo-enhancement) depends on the lesion size and location, the background parenchymal attenuation, the number of the detectors and tube voltage (102, 114).

Another typical example is the assessment of the incidental adrenal lesions. According to recent guidelines (115), a 10 HU threshold is applied on non-contrast CT to decide the further work-up procedures. If the density of a lesion is below the 10 HU cut-off, it is considered as benign adenoma; otherwise, a dedicated adrenal CT is recommended based on the size of the lesion and prior imaging or cancer history of the patient. A further example of the HU-based diagnosis is the assessment of the cardiovascular risk with the Agatson score (116).

5.3 Comparison of different CA application protocols for cardiovascular thoracic CT in young children

Thoracic CT angiography is one of the most challenging tasks in the pediatric radiology. On one hand, a sufficient enhancement of all cardiovascular thoracic structures, including the right- and left heart-chambers as well as the systemic and pulmonary main vessels is essential, especially in young children. On the other hand, CT acquisition needs to be adjusted to the unique anatomical and physiological characteristics of the young children, as introduced in chapter 1.2. Several CT application protocols were suggested in the literature to overcome these difficulties, as presented in chapter 1.4.2. However, comparative studies on the resulted image quality and diagnostic competencies are still lacking.

The retrospective comparison of thoracic CT examinations in children younger than two years revealed that the MBT technique is sufficient to achieve a homogenous enhancement in the systemic and pulmonary main vessels. This is, however, achieved by injecting less CA compared to the other two protocols. While the objective parameters of image quality were comparable between all three injection protocols (**Figures 22 and 23**), examinations with MBT were rated with the highest scores in the subjective image analysis (**Table 15**). The main influencing parameters of the image contrast, such as tube voltage and the iodinated CA concentration, were standardized. This allowed a reliable comparison of the different CA application protocols. Although the total CA saving by MBT protocol might seem negligible, we believe, that every tiny amount of the CA reduction matters, which is even more meaningful in light of the latest results demonstrating the relation between iodine amount and the radiation-induced DNA double-strand breakages (76).

As introduced in chapter 1.4.2, with MBT technique, the specially programmed dual-chamber power injector releases 1 ml CA and 2 ml saline alternating, which results in a CA dilution during the CA application. The prolonged CA application allows the simultaneous enhancement of all systemic and pulmonary vascular structures and prevents perivascular streak artifacts more effectively.

The maximal applied CA volume is calculated individually according to patient weight before the examination. The operator controls the CA application process actively with the option to stop the power injector before the maximal CA volume is injected. This active control allows more space for further CA reduction in comparison to the other CA protocols with CA dilution, where the dilution occurs before the injection. Choo et al. examined 77 children (mean age 6.4 months ranging between 5 days and 5 years) with suspected airway obstruction (60), while Kim et al. performed thoracic CTA on 14 children (median age 2.3 months, ranging from 3 days to 8 months) with surgical corrected TAPVR (49). In both patient populations, CA was diluted before the CA application with an equal volume of saline and was injected by a mechanical power injector. None of the mentioned studies with pre-diluted CA has reported the injected CA amount. Goo et al. applied a similar CA dilution approach in the triphasic CA protocol with 50% and 10% CA dilution, as described in chapter 1.4.2 (41).

Several studies have examined the clinical utility of a CA with reduced iodine load. Wang et al. conducted cardiac CTs in 44 patients (mean age 8.1 ± 4.3 months, weight 7.3 ± 1.4 kg) with congenital heart disease by injecting 1-1.5 ml/kg CA with 270 mg iodine/ml in a dual-phase protocol (117). The cardiac CT examinations were conducted on a 64-slice CT with 80 kV tube potential, 120 mAs tube current, and adaptive iterative reconstruction. The authors reported a high diagnostic accuracy with a mean iodine load of 3.9 ± 0.8 g. Because of the similar patient age and weight, this study is well comparable with our study cohort. Despite the larger examination area (thoracic vs. cardiac CT), patients with the MBT technique received less iodine load (2.7 ± 1.1 g iodine) with similar results regarding the subjective image analysis. Due to the different CNR calculation approaches as well as the missing values of mean vascular enhancement, the objective image qualities are difficult to compare. However, the reported image noise was comparable in both studies.

Hou et al. (92) conducted a study with a highly similar patient population to that of Wang et al. (117), who underwent cardiac CT. These patients received CA either with 270 mg iodine/ml or with 370 mg iodine/ml. The reported iodine load was similar, as in the previously discussed study (3.9 ± 7.5 g iodine vs. 5.8 ± 1.0 g iodine) (117). This range is, however, highly exceeds the iodine load of our patients scanned with MBT (2.7 ± 1.1 g iodine), with comparable mean enhancement and image noise.

Hwang et al. performed a similar study with the inclusion of younger patients who underwent cardiac CT with congenital cardiac disorders (118). According to the concentration of the injected CA (270 mg vs. 370 mg iodine/ml), patients were divided into two groups (age and weight in group I and II as follows: 44.9 ±78.6 days and 3.9 ± 1.8 kg as well as 45.3 ± 75.2 days and 4.1 ± 1.9 kg, respectively). CT examinations were conducted with 80 kV tube voltage and with fixed (empirical) bolus delay. The achieved mean enhancement was slightly above that of reached by MBT with good overall image quality. However, the injected CA was less in the study of Hwang et al. (injected CA in group I and II as follows: 7.8 ± 3.5 ml and 7.9 ± 3.5 ml, respectively, receiving 2 ml CA pro kg), compared to the examinations with MBT protocol (9.0 ± 3.7 ml which means 1.8 ± 0.7 ml/kg). The slightly younger patient population might explain this difference between the study of Hwang et al. and our study.

The third-generation dual-source CT opened a further opportunity to reduce the iodinated CA amount. In dual-energy mode, the low tube voltage (70 kV) allows CA volume saving by generating X-rays close to the k-edge of the iodine (33.2 keV), which improves the iodine contrast (46). Despite the promising case reports, comparative studies on the absolute CA saving are still lacking.

5.4 Comparison of the applied radiation in a retrospective evaluation of the three different CA application protocols

Despite all efforts, the comparison of radiation exposure parameters between the CT examinations with different CA application protocols in such a retrospective setting was not possible. The most important limiting factor is the technical progress during the long study period with the introduction of the iterative reconstruction. Even if the study groups were tailored whether iterative reconstruction was performed or not, the limited number of patients would impair the comparison. However, as indicated in **Table 12**, we found no significant difference between the groups regarding radiation exposure. A closer analysis of the exposure parameters revealed a significantly less tube current in the MBT group than in the other groups. However, the recorded image noise was significantly less, as well. This virtual paradox might be explained by a higher percentage of the iterative reconstruction as well as the 3 mm slice thickness in the MBT group since both parameters similarly influence the image noise allowing a further reduction of the tube current.

Due to the technical diversity of the CT scanners, the comparison of the delivered radiation dose to other related studies is challenging. However, the measured radiation doses are comparable with the European and German DRLs (19, 119).

5.5 Limitations

Both described studies bear several limitations. In the phantom study, the proposed ABT thresholds were estimated based solely on phantom measurements. To verify their applicability, further clinical studies are required in animals and humans. To generalize the recommended ABT thresholds, phantom scans should also be performed in a wider variety of CT scanners, other than those three in our institution. In the course of CT scan protocol standardization, the vendor-specific hard- and software specifications should also be considered.

Despite the very long study period, the small patient population was an important limitation of the presented retrospective study on pediatric patients. A further limitation was the heterogeneity of the small patient collective regarding the underlying diseases and the high variability of clinical cases. The wide variety of congenital heart diseases might also have had an influence on the hemodynamic status and, thus, on the measured attenuation in the heart chamber and great vessels. In the course of the long study period several hardware and software updates took place. As a consequence, the comparison of radiation exposure (as discussed in chapter 5.4) was not possible. Unfortunately, kidney function parameters after the CTA scans were not recorded. Therefore, the assumed nephroprotective effect of the MBT protocol by reducing the applied CA volume could not have been verified. The influence of the location and size of the venous line on the enhancement pattern was not considered either.

6. Concluding remarks

The primary focus of the current work was to elaborate some specific, challenging aspects of CA application in pediatric cardiothoracic CTA imaging in order to optimize image quality. Based on phantom measurements and using a transparent and reproducible computing approach, ABT threshold values were proposed to avoid inappropriate CA timing at reduced tube voltages. Furthermore, the comparison of three different CA application protocols revealed some advantages favoring MBT regarding the reduction of CA volume and improvement of image quality. This encourages the further clinical application of the MBT protocol.

7. References

1. ACR–ASER–SCBT-MR–SPR PRACTICE PARAMETER FOR THE PERFORMANCE OF PEDIATRIC COMPUTED TOMOGRAPHY (CT)2019. Available from: https://www.acr.org/-/media/ACR/Files/Practice-Parameters/CT-Ped.pdf.

2. Stagnaro N, Rizzo F, Torre M, Cittadini G, Magnano G. Multimodality imaging of pediatric airways disease: indication and technique. Radiol Med. 2017;122(6):419-29.

3. Newman B, Callahan MJ. ALARA (as low as reasonably achievable) CT 2011--executive summary. Pediatr Radiol. 2011;41 Suppl 2:453-5.

4. Andronikou S, Goussard P, Sorantin E. Computed tomography in children with community-acquired pneumonia. Pediatr Radiol. 2017;47(11):1431-40.

5. Dishop MK, Kuruvilla S. Primary and metastatic lung tumors in the pediatric population: a review and 25-year experience at a large children's hospital. Arch Pathol Lab Med. 2008;132(7):1079-103.

6. Weiser DA, Kaste SC, Siegel MJ, Adamson PC. Imaging in childhood cancer: a Society for Pediatric Radiology and Children's Oncology Group Joint Task Force report. Pediatr Blood Cancer. 2013;60(8):1253-60.

7. Lobo L, Antunes D. Chest CT in infants and children. Eur J Radiol. 2013;82(7):1108-17.

8. Piccolo CL, Ianniello S, Trinci M, Galluzzo M, Tonerini M, Zeccolini M, et al. Diagnostic Imaging in pediatric thoracic trauma. Radiol Med. 2017;122(11):850-65.

9. Semple TR, Ashworth MT, Owens CM. Interstitial Lung Disease in Children Made Easier...Well, Almost. Radiographics. 2017;37(6):1679-703.

10. Hirsch FW, Sorge I, Vogel-Claussen J, Roth C, Grafe D, Pats A, et al. The current status and further prospects for lung magnetic resonance imaging in pediatric radiology. Pediatr Radiol. 2020;50(5):734-49.

11. Zirpoli S, Munari AM, Primolevo A, Scarabello M, Costanzo S, Farolfi A, et al. Agreement between magnetic resonance imaging and computed tomography in the postnatal evaluation of congenital lung malformations: a pilot study. Eur Radiol. 2019;29(9):4544-54.

12. Sorantin E, Weissensteiner S, Hasenburger G, Riccabona M. CT in children--dose protection and general considerations when planning a CT in a child. Eur J Radiol. 2013;82(7):1043-9.

13. Brenner D, Elliston C, Hall E, Berdon W. Estimated risks of radiation-induced fatal cancer from pediatric CT. AJR Am J Roentgenol. 2001;176(2):289-96.

14. Goske MJ, Phillips RR, Mandel K, McLinden D, Racadio JM, Hall S. Image gently: a web-based practice quality improvement program in CT safety for children. AJR Am J Roentgenol. 2010;194(5):1177-82.

15. Parakh A, Kortesniemi M, Schindera ST. CT Radiation Dose Management: A Comprehensive Optimization Process for Improving Patient Safety. Radiology. 2016;280(3):663-73.

16. Winkler NT. ALARA concept--now a requirement. Radiol Technol. 1980;51(4):525.

17. Diagnostic reference levels in medical imaging: review and additional advice. Ann ICRP. 2001;31(4):33-52.

18. Billinger J, Nowotny R, Homolka P. Diagnostic reference levels in pediatric radiology in Austria. Eur Radiol. 2010;20(7):1572-9.

19. Schegerer A, Loose R, Heuser LJ, Brix G. Diagnostic Reference Levels for Diagnostic and Interventional X-Ray Procedures in Germany: Update and Handling. Rofo. 2019;191(8):739-51.

20. Strauss KJ, Somasundaram E, Sengupta D, Marin JR, Brady SL. Radiation Dose for Pediatric CT: Comparison of Pediatric versus Adult Imaging Facilities. Radiology. 2019;291(1):158-67.

21. Paterson A, Frush DP. Dose reduction in paediatric MDCT: general principles. Clin Radiol. 2007;62(6):507-17.

22. Nievelstein RA, van Dam IM, van der Molen AJ. Multidetector CT in children: current concepts and dose reduction strategies. Pediatr Radiol. 2010;40(8):1324-44.

23. Goo HW. Individualized volume CT dose index determined by cross-sectional area and mean density of the body to achieve uniform image noise of contrast-enhanced pediatric chest

CT obtained at variable kV levels and with combined tube current modulation. Pediatr Radiol. 2011;41(7):839-47.

24. Siegel MJ, Hildebolt C, Bradley D. Effects of automated kilovoltage selection technology on contrast-enhanced pediatric CT and CT angiography. Radiology. 2013;268(2):538-47.

25. Brink M, de Lange F, Oostveen LJ, Dekker HM, Kool DR, Deunk J, et al. Arm raising at exposure-controlled multidetector trauma CT of thoracoabdominal region: higher image quality, lower radiation dose. Radiology. 2008;249(2):661-70.

26. Cody DD. Management of auto exposure control during pediatric computed tomography. Pediatr Radiol. 2014;44 Suppl 3:427-30.

27. Ryu YJ, Choi YH, Cheon JE, Park JE, Kim WS, Kim IO. Effect of arm position, presence of medical devices, and off-centering during acquisition of scout image on automatic tube voltage selection and current modulation in pediatric chest CT. PLoS One. 2018;13(4):e0195807.

28. Goo HW, Suh DS. Tube current reduction in pediatric non-ECG-gated heart CT by combined tube current modulation. Pediatr Radiol. 2006;36(4):344-51.

29. Greess H, Wolf H, Baum U, Lell M, Pirkl M, Kalender W, et al. Dose reduction in computed tomography by attenuation-based on-line modulation of tube current: evaluation of six anatomical regions. Eur Radiol. 2000;10(2):391-4.

30. Nelson TR. Practical strategies to reduce pediatric CT radiation dose. J Am Coll Radiol. 2014;11(3):292-9.

31. Deak PD, Langner O, Lell M, Kalender WA. Effects of adaptive section collimation on patient radiation dose in multisection spiral CT. Radiology. 2009;252(1):140-7.

32. Stiller W. Basics of iterative reconstruction methods in computed tomography: A vendor-independent overview. Eur J Radiol. 2018;109:147-54.

33. Brady SL, Moore BM, Yee BS, Kaufman RA. Pediatric CT: implementation of ASIR for substantial radiation dose reduction while maintaining pre-ASIR image noise. Radiology. 2014;270(1):223-31.

34. Katsura M, Matsuda I, Akahane M, Sato J, Akai H, Yasaka K, et al. Model-based iterative reconstruction technique for radiation dose reduction in chest CT: comparison with the adaptive statistical iterative reconstruction technique. Eur Radiol. 2012;22(8):1613-23.

35. Katsura M, Sato J, Akahane M, Matsuda I, Ishida M, Yasaka K, et al. Comparison of pure and hybrid iterative reconstruction techniques with conventional filtered back projection: image quality assessment in the cervicothoracic region. Eur J Radiol. 2013;82(2):356-60.

36. O'Connor M FS. Conference paper: Noise variations across clinically accepted paediatric body CT scans European Congress of Radiology Mar; Vienna2016. p. 162-465.

37. Honnef D, Mahnken AH, Haras G, Wildberger JE, Staatz G, Das M, et al. Pediatric multidetector computed tomography using tube current modulation and a patient image gallery. Acta Radiol. 2008;49(4):475-83.

38. Karmazyn B, Liang Y, Ai H, Eckert GJ, Cohen MD, Wanner MR, et al. Optimization of hybrid iterative reconstruction level in pediatric body CT. AJR Am J Roentgenol. 2014;202(2):426-31.

39. Kim JH, Kim MJ, Kim HY, Lee MJ. Radiation dose reduction and image quality in pediatric abdominal CT with kVp and mAs modulation and an iterative reconstruction technique. Clin Imaging. 2014;38(5):710-4.

40. Singh S, Kalra MK, Shenoy-Bhangle AS, Saini A, Gervais DA, Westra SJ, et al. Radiation dose reduction with hybrid iterative reconstruction for pediatric CT. Radiology. 2012;263(2):537-46.

41. Goo HW. State-of-the-art CT imaging techniques for congenital heart disease. Korean J Radiol. 2010;11(1):4-18.

42. Schindler P, Kehl HG, Wildgruber M, Heindel W, Schulke C. Cardiac CT in the Preoperative Diagnostics of Neonates with Congenital Heart Disease: Radiation Dose Optimization by Omitting Test Bolus or Bolus Tracking. Academic radiology. 2020;27(5):e102-e8.

43. Ishikawa Y, Urikura A, Yoshida T, Takiguchi K, Nakaya Y. Radiation dose optimization for the bolus tracking technique in abdominal computed tomography: usefulness of real-time iterative reconstruction for monitoring scan. Radiol Phys Technol. 2017;10(2):155-60.

44. Matsumoto JKN, Assuncao-Jr AN, Dantas Junior RN, Araujo-Filho JAB, Andrade SS, Nomura CH, et al. Radiation dose reduction by adjusting bolus tracking parameters in a 320-detector row scanner. J Cardiovasc Comput Tomogr. 2018;12(4):312-5.

45. Mitchell DP, Rowan M, Loughman E, Ridge CA, MacMahon PJ. Contrast monitoring techniques in CT pulmonary angiography: An important and underappreciated contributor to breast dose. Eur J Radiol. 2017;86:184-9.

46. Schicchi N, Fogante M, Esposto Pirani P, Agliata G, Basile MC, Oliva M, et al. Third-generation dual-source dual-energy CT in pediatric congenital heart disease patients: state-of-the-art. Radiol Med. 2019;124(12):1238-52.

47. Boone JM SK, Cody DD, McCollough CH, McNitt-Gray MF, Toth TL. Size-Specific Dose Estimates (SSDE) in Pediatric and Adult Body CT Examination. . College Park, MD: American Association of Physicists in Medicine. 2011.

48. Young C, Xie C, Owens CM. Paediatric multi-detector row chest CT: what you really need to know. Insights Imaging. 2012;3(3):229-46.

49. Kim THea. Helical CT angiography and three-dimensional reconstruction of total anomalous pulmonary venous connections in neonates and infants. AJR 2000(175):1381–6.

50. Schooler GR, Zurakowski D, Lee EY. Evaluation of contrast injection site effectiveness: thoracic CT angiography in children with hand injection of IV contrast material. AJR Am J Roentgenol. 2015;204(2):423-7.

51. Zhong YM, Jaffe RB, Liu JF, Sun AM, Gao W, Wang Q, et al. Multi-slice computed tomography assessment of bronchial compression with absent pulmonary valve. Pediatr Radiol. 2014;44(7):803-9.

52. Sandler KL, Markham LW, Mah ML, Byrum EP, Williams JR. Optimizing CT angiography in patients with Fontan physiology: single-center experience of dual-site power injection. Clin Radiol. 2014;69(12):e562-7.

53. Rigsby CK, McKenney SE, Hill KD, Chelliah A, Einstein AJ, Han BK, et al. Radiation dose management for pediatric cardiac computed tomography: a report from the Image Gently 'Have-A-Heart' campaign. Pediatr Radiol. 2018;48(1):5-20.

54. Amaral JG, Traubici J, BenDavid G, Reintamm G, Daneman A. Safety of power injector use in children as measured by incidence of extravasation. AJR Am J Roentgenol. 2006;187(2):580-3.

55. Yang M, Mo XM, Jin JY, Zhang J, Liu B, Wu M, et al. Image quality and radiation exposure in pediatric cardiovascular CT angiography from different injection sites. AJR Am J Roentgenol. 2011;196(2):W117-22.

56. Cademartiri F, Nieman K, van der Lugt A, Raaijmakers RH, Mollet N, Pattynama PM, et al. Intravenous contrast material administration at 16-detector row helical CT coronary angiography: test bolus versus bolus-tracking technique. Radiology. 2004;233(3):817-23.

57. Trinavarat P. Computed tomographic angiography (CTA) of major thoracic vessels in children--a pictorial assay on common findings also discussing CTA technique. Eur J Radiol. 2013;82(7):1083-90.

58. Scialpi M, Schiavone, R., D'Andrea, A., Palumbo, I., Magli, M. et al. . Single-phase Whole-body 64-MDCT Split-bolus Protocol for Pediatric Oncology: Diagnostic Efficacy and Dose Radiation. Anticancer Res. 2015;35(5):3041-8.

59. Wang X, Zhong Y, Hu L, Xue L, Shi M, Qiu H, et al. A prospective evaluation of the contrast, radiation dose and image quality of contrast-enhanced CT scans of paediatric abdomens using a low-concentration iodinated contrast agent and low tube voltage combined with 70% ASIR algorithm. Int J Clin Pract. 2016;70 Suppl 9B:B16-21.

60. Choo KS, Lee HD, Ban JE, Sung SC, Chang YH, Kim CW, et al. Evaluation of obstructive airway lesions in complex congenital heart disease using composite volume-rendered images from multislice CT. Pediatr Radiol. 2006;36(3):219-23.

61. Nagy E, Tschauner S, Marterer R, Riedl R, Sorantin E. Chest CTA in children younger than two years - a retrospective comparison of three contrast injection protocols. Sci Rep. 2019;9(1):18109.

62. Ghadimi Mahani M, Agarwal PP, Rigsby CK, Lu JC, Fazeli Dehkordy S, Wright RA, et al. CT for Assessment of Thrombosis and Pulmonary Embolism in Multiple Stages of Single-Ventricle Palliation: Challenges and Suggested Protocols. Radiographics. 2016;36(5):1273-84.

63. Park EA, Lee W, Chung SY, Yin YH, Chung JW, Park JH. Optimal scan timing and intravenous route for contrast-enhanced computed tomography in patients after Fontan operation. J Comput Assist Tomogr. 2010;34(1):75-81.

64. Prabhu SP, Mahmood S, Sena L, Lee EY. MDCT evaluation of pulmonary embolism in children and young adults following a lateral tunnel Fontan procedure: optimizing contrast-enhancement techniques. Pediatr Radiol. 2009;39(9):938-44.

65. Wilhelm-Leen E, Montez-Rath ME, Chertow G. Estimating the Risk of Radiocontrast-Associated Nephropathy. J Am Soc Nephrol. 2017;28(2):653-9.

66. Bedoya MA, White AM, Edgar JC, Pradhan M, Raab EL, Meyer JS. Effect of Intravenous Administration of Contrast Media on Serum Creatinine Levels in Neonates. Radiology. 2017;284(2):530-40.

67. Carlo WF, Clark ST, Borasino S, Alten JA. Impact of contrast exposure from computed tomography angiography on acute kidney injury after neonatal cardiopulmonary bypass surgery. Congenit Heart Dis. 2017;12(4):540-5.

68. McDonald JS, McDonald RJ, Tran CL, Kolbe AB, Williamson EE, Kallmes DF. Postcontrast Acute Kidney Injury in Pediatric Patients: A Cohort Study. Am J Kidney Dis. 2018;72(6):811-8.

69. Cantais A, Hammouda Z, Mory O, Patural H, Stephan JL, Gulyaeva L, et al. Incidence of contrast-induced acute kidney injury in a pediatric setting: a cohort study. Pediatr Nephrol. 2016;31(8):1355-62.

70. Friebe M. Computed tomography and magnetic resonance imaging contrast media injectors: technical feature review - what is really needed? Med Devices (Auckl). 2016;9:231-9.

71. Callahan MJ, Servaes S, Lee EY, Towbin AJ, Westra SJ, Frush DP. Practice patterns for the use of iodinated i.v. contrast media for pediatric CT studies: a survey of the Society for Pediatric Radiology. AJR Am J Roentgenol. 2014;202(4):872-9.

72. Kuefner MA, Brand M, Engert C, Schwab SA, Uder M. Radiation Induced DNA Double-Strand Breaks in Radiology. Rofo. 2015;187(10):872-8.

73. Deinzer CK, Danova D, Kleb B, Klose KJ, Heverhagen JT. Influence of different iodinated contrast media on the induction of DNA double-strand breaks after in vitro X-ray irradiation. Contrast Media Mol Imaging. 2014;9(4):259-67.

74. Pathe C, Eble K, Schmitz-Beuting D, Keil B, Kaestner B, Voelker M, et al. The presence of iodinated contrast agents amplifies DNA radiation damage in computed tomography. Contrast Media Mol Imaging. 2011;6(6):507-13.

75. Wang L, Li Q, Wang XM, Hao GY, Jie B, Hu S, et al. Enhanced radiation damage caused by iodinated contrast agents during CT examination. Eur J Radiol. 2017;92:72-7.

76. Van Cauteren T, Honoria Da Silva E, Van Gompel G, Kersemans V, Sermon K, de Mey J, et al. Iodine Dose of Administered Contrast Media Affects the Level of Radiation-Induced DNA Damage During Cardiac CT Scans. AJR Am J Roentgenol. 2019;213(2):404-9.

77. Jevtovic-Todorovic V, Hartman RE, Izumi Y, Benshoff ND, Dikranian K, Zorumski CF, et al. Early exposure to common anesthetic agents causes widespread neurodegeneration in the developing rat brain and persistent learning deficits. J Neurosci. 2003;23(3):876-82.

78. DiMaggio C, Sun LS, Li G. Early childhood exposure to anesthesia and risk of developmental and behavioral disorders in a sibling birth cohort. Anesth Analg. 2011;113(5):1143-51.

79. Ing C, Sun M, Olfson M, DiMaggio CJ, Sun LS, Wall MM, et al. Age at Exposure to Surgery and Anesthesia in Children and Association With Mental Disorder Diagnosis. Anesth Analg. 2017;125(6):1988-98.

80. Zhang H, Du L, Du Z, Jiang H, Han D, Li Q. Association between childhood exposure to single general anesthesia and neurodevelopment: a systematic review and meta-analysis of cohort study. J Anesth. 2015;29(5):749-57.

81. Flick RP, Katusic SK, Colligan RC, Wilder RT, Voigt RG, Olson MD, et al. Cognitive and behavioral outcomes after early exposure to anesthesia and surgery. Pediatrics. 2011;128(5):e1053-61.

82. Wang X, Xu Z, Miao CH. Current clinical evidence on the effect of general anesthesia on neurodevelopment in children: an updated systematic review with meta-regression. PLoS One. 2014;9(1):e85760.

83. FDA Drug Safety Communication: FDA approves label changes for use of general anesthetic and sedation drugs in young children Available at: https://www.fda.gov/Drugs/DrugSafety/ucm554634.htm.. [

84. McCann ME, de Graaff JC, Dorris L, Disma N, Withington D, Bell G, et al. Neurodevelopmental outcome at 5 years of age after general anaesthesia or awake-regional anaesthesia in infancy (GAS): an international, multicentre, randomised, controlled equivalence trial. Lancet. 2019;393(10172):664-77.

85. Han BK, Overman DM, Grant K, Rosenthal K, Rutten-Ramos S, Cook D, et al. Non-sedated, free breathing cardiac CT for evaluation of complex congenital heart disease in neonates. J Cardiovasc Comput Tomogr. 2013;7(6):354-60.

86. Lell MM, May M, Deak P, Alibek S, Kuefner M, Kuettner A, et al. High-pitch spiral computed tomography: effect on image quality and radiation dose in pediatric chest computed tomography. Invest Radiol. 2011;46(2):116-23.

87. Kim SH, Choi YH, Cho HH, Lee SM, Shin SM, Cheon JE, et al. Comparison of Image Quality and Radiation Dose between High-Pitch Mode and Low-Pitch Mode Spiral Chest CT in Small Uncooperative Children: The Effect of Respiratory Rate. Eur Radiol. 2016;26(4):1149-58.

88. Kino A, Zucker EJ, Honkanen A, Kneebone J, Wang J, Chan F, et al. Ultrafast pediatric chest computed tomography: comparison of free-breathing vs. breath-hold imaging with and without anesthesia in young children. Pediatr Radiol. 2019;49(3):301-7.

89. Sande EP, Martinsen AC, Hole EO, Olerud HM. Interphantom and interscanner variations for Hounsfield units--establishment of reference values for HU in a commercial QA phantom. Phys Med Biol. 2010;55(17):5123-35.

90. Sorantin E, Riccabona M, Stucklschweiger G, Guss H, Fotter R. Experience with volumetric (320 rows) pediatric CT. Eur J Radiol. 2013;82(7):1091-7.

91. Newell JD, Jr., Fuld MK, Allmendinger T, Sieren JP, Chan KS, Guo J, et al. Very low-dose (0.15 mGy) chest CT protocols using the COPDGene 2 test object and a third-generation dual-source CT scanner with corresponding third-generation iterative reconstruction software. Invest Radiol. 2015;50(1):40-5.

92. Hou QR, Gao W, Sun AM, Wang Q, Qiu HS, Wang F, et al. A prospective evaluation of contrast and radiation dose and image quality in cardiac CT in children with complex congenital heart disease using low-concentration iodinated contrast agent and low tube voltage and current. Br J Radiol. 2017;90(1070):20160669.

93. Szucs-Farkas Z, Strautz T, Patak MA, Kurmann L, Vock P, Schindera ST. Is body weight the most appropriate criterion to select patients eligible for low-dose pulmonary CT angiography? Analysis of objective and subjective image quality at 80 kVp in 100 patients. Eur Radiol. 2009;19(8):1914-22.

94. Barrett JF, Keat N. Artifacts in CT: recognition and avoidance. Radiographics. 2004;24(6):1679-91.

95. Lee EY, Siegel MJ, Hildebolt CF, Gutierrez FR, Bhalla S, Fallah JH. MDCT evaluation of thoracic aortic anomalies in pediatric patients and young adults: comparison of axial, multiplanar, and 3D images. AJR Am J Roentgenol. 2004;182(3):777-84.

96. Leschka S, Oechslin E, Husmann L, Desbiolles L, Marincek B, Genoni M, et al. Pre- and postoperative evaluation of congenital heart disease in children and adults with 64-section CT. Radiographics. 2007;27(3):829-46.

97. Ho KM. Using linear regression to assess dose-dependent bias on a Bland-Altman plot. Journal of Emergency and Critical Care Medicine. 2018;2(8).

98. Shen Y, Hu X, Zou X, Zhu D, Li Z, Hu D. Did low tube voltage CT combined with low contrast media burden protocols accomplish the goal of "double low" for patients? An overview of applications in vessels and abdominal parenchymal organs over the past 5 years. Int J Clin Pract. 2016;70 Suppl 9B:B5-B15.

99. Zapala MA, Zurakowski D, Lee EY. Comparison of Mechanical Versus Hand Administration of IV Contrast Agents for Pediatric Pulmonary CT Angiography. AJR Am J Roentgenol. 2017;208(3):632-6.

100. Yao Q, Hu X, Pa M, Huang G. Non-ECG-gated MDCTA of infracardiac total anomalous pulmonary venous connection in neonates and young infants. Herz. 2013;38(5):539-43.

101. Thust SC, Chong WK, Gunny R, Mazumder A, Poitelea M, Welsh A, et al. Paediatric cerebrovascular CT angiography-towards better image quality. Quant Imaging Med Surg. 2014;4(6):469-74.

102. Birnbaum BA, Hindman N, Lee J, Babb JS. Multi-detector row CT attenuation measurements: assessment of intra- and interscanner variability with an anthropomorphic body CT phantom. Radiology. 2007;242(1):109-19.

103. Cao X, Jin C, Tan T, Guo Y. Optimal threshold in low-dose CT quantification of emphysema. Eur J Radiol. 2020;129:109094.

104. Chen-Mayer HH, Fuld MK, Hoppel B, Judy PF, Sieren JP, Guo J, et al. Standardizing CT lung density measure across scanner manufacturers. Med Phys. 2017;44(3):974-85.

105. Eggermont F, Verdonschot N, van der Linden Y, Tanck E. Calibration with or without phantom for fracture risk prediction in cancer patients with femoral bone metastases using CT-based finite element models. PLoS One. 2019;14(7):e0220564.

106. Mao SS, Li D, Luo Y, Syed YS, Budoff MJ. Application of quantitative computed tomography for assessment of trabecular bone mineral density, microarchitecture and mechanical property. Clin Imaging. 2016;40(2):330-8.

107. Regan EA, Lynch DA, Curran-Everett D, Curtis JL, Austin JH, Grenier PA, et al. Clinical and Radiologic Disease in Smokers With Normal Spirometry. JAMA Intern Med. 2015;175(9):1539-49.

108. Kim YW, Kim JH, Yoon SH, Lee JH, Lee CH, Shin CS, et al. Vertebral bone attenuation on low-dose chest CT: quantitative volumetric analysis for bone fragility assessment. Osteoporos Int. 2017;28(1):329-38.

109. Beland MD, Scappaticci AA, Machan JT, Huda W, Collins SA, Mayo-Smith WW. Effect of patient size on mean sterile water attenuation during multiphase CT examinations. AJR Am J Roentgenol. 2013;200(5):1048-53.

110. Lamba R, McGahan JP, Corwin MT, Li CS, Tran T, Seibert JA, et al. CT Hounsfield numbers of soft tissues on unenhanced abdominal CT scans: variability between two different manufacturers' MDCT scanners. AJR Am J Roentgenol. 2014;203(5):1013-20.

111. Patel N, Li D, Nakanishi R, Fatima B, Andreini D, Pontone G, et al. Comparison of Whole Heart Computed Tomography Scanners for Image Quality Lower Radiation Dosing in Coronary Computed Tomography Angiography: The CONVERGE Registry. Academic radiology. 2019;26(11):1443-9.

112. Cropp RJ, Seslija P, Tso D, Thakur Y. Scanner and kVp dependence of measured CT numbers in the ACR CT phantom. J Appl Clin Med Phys. 2013;14(6):4417.

113. Silverman SG, Pedrosa I, Ellis JH, Hindman NM, Schieda N, Smith AD, et al. Bosniak Classification of Cystic Renal Masses, Version 2019: An Update Proposal and Needs Assessment. Radiology. 2019;292(2):475-88.

114. Wang ZJ, Coakley FV, Fu Y, Joe BN, Prevrhal S, Landeras LA, et al. Renal cyst pseudoenhancement at multidetector CT: what are the effects of number of detectors and peak tube voltage? Radiology. 2008;248(3):910-6.

115. Mayo-Smith WW, Song JH, Boland GL, Francis IR, Israel GM, Mazzaglia PJ, et al. Management of Incidental Adrenal Masses: A White Paper of the ACR Incidental Findings Committee. J Am Coll Radiol. 2017;14(8):1038-44.

116. Nelson JC, Kronmal RA, Carr JJ, McNitt-Gray MF, Wong ND, Loria CM, et al. Measuring coronary calcium on CT images adjusted for attenuation differences. Radiology. 2005;235(2):403-14.

117. Wang SY, Gao W, Zhong YM, Sun AM, Wang Q, Hu LW, et al. Prospective ECG-triggering cardiac CT for infants with complex congenital heart disease using low-dose contrast medium, low tube voltage, and adaptive statistical iterative reconstruction. Clin Radiol. 2017;72(6):502-7.

118. Hwang JY, Choo KS, Choi YY, Kim JH, Ryu H, Han J, et al. Subjective and objective image differences in pediatric computed tomography cardiac angiography using lower iodine concentration. Pediatr Radiol. 2017;47(6):701-9.

119. Granata C, Sorantin E, Seuri R, Owens CM. European Society of Paediatric Radiology Computed Tomography and Dose Task Force: European guidelines on diagnostic reference levels for paediatric imaging. Pediatr Radiol. 2019;49(5):702-5.